Iowa State University
Digital Repository

Retrospective Theses and Dissertations | Iowa State University Capstones, Theses and Dissertations

1995

Growth optimization and characterization of gallium indium nitride grown by electron-cyclotron-resonance plasma-assisted molecular-beam epitaxy

William O. Liners
Iowa State University

Follow this and additional works at: https://lib.dr.iastate.edu/rtd

Part of the Electrical and Electronics Commons, and the Materials Science and Engineering Commons

Recommended Citation

Liners, William O., "Growth optimization and characterization of gallium indium nitride grown by electron-cyclotron-resonance plasma-assisted molecular-beam epitaxy " (1995). *Retrospective Theses and Dissertations*. 11069.
https://lib.dr.iastate.edu/rtd/11069

This Dissertation is brought to you for free and open access by the Iowa State University Capstones, Theses and Dissertations at Iowa State University Digital Repository. It has been accepted for inclusion in Retrospective Theses and Dissertations by an authorized administrator of Iowa State University Digital Repository. For more information, please contact digirep@iastate.edu.

المنارة للاستشارات

www.manaraa.com

INFORMATION TO USERS

This manuscript has been reproduced from the microfilm master. UMI films the text directly from the original or copy submitted. Thus, some thesis and dissertation copies are in typewriter face, while others may be from any type of computer printer.

The quality of this reproduction is dependent upon the quality of the copy submitted. Broken or indistinct print, colored or poor quality illustrations and photographs, print bleedthrough, substandard margins, and improper alignment can adversely affect reproduction.

In the unlikely event that the author did not send UMI a complete manuscript and there are missing pages, these will be noted. Also, if unauthorized copyright material had to be removed, a note will indicate the deletion.

Oversize materials (e.g., maps, drawings, charts) are reproduced by sectioning the original, beginning at the upper left-hand corner and continuing from left to right in equal sections with small overlaps. Each original is also photographed in one exposure and is included in reduced form at the back of the book.

Photographs included in the original manuscript have been reproduced xerographically in this copy. Higher quality 6" x 9" black and white photographic prints are available for any photographs or illustrations appearing in this copy for an additional charge. Contact UMI directly to order.

UMI

A Bell & Howell Information Company
300 North Zeeb Road, Ann Arbor, MI 48106-1346 USA
313/761-4700 800/521-0600

Growth optimization and characterization of gallium indium nitride grown by electron-cyclotron-resonance plasma-assisted molecular-beam epitaxy

by

William O. Liners

A Dissertation Submitted to the
Graduate Faculty in Partial Fulfillment of
the Requirement for the Degree of
DOCTOR OF PHILOSOPHY

Department: Electrical and Computer Engineering
Major: Electrical Engineering (Microelectronics)

Approved:

Signature was redacted for privacy.

In Charge of Major Work

Signature was redacted for privacy.

For the Major Department

Signature was redacted for privacy.

For the Graduate College

Iowa State University
Ames, Iowa
1995

UMI Number: 9610970

UMI Microform 9610970
Copyright 1996, by UMI Company. All rights reserved.

This microform edition is protected against unauthorized
copying under Title 17, United States Code.

UMI
300 North Zeeb Road
Ann Arbor, MI 48103

To my wife, Kathleen Marie Liners

my son, Thomas

my parents, Hank and Vivian

and to my in-laws, Pat and Andy.

Without whom this work would not be possible.

TABLE OF CONTENTS

I. INTRODUCTION 1

I.1 Project Description 1

I.2 Important Properties of III-V Nitrides 4

I.2.1 Refractory Nitrides 4

I.2.2 III-V Nitride Phases 6

I.3 Previous Work 7

I.3.1 Gallium Nitride 7

I.3.2 Indium Containing Nitrides 8

I.3.3 Devices 8

I.4 Potential Applications 10

II. EXPERIMENTAL 12

II.1 ECR-MBE 12

II.2 Substrate Preparation 15

II.3 Growth Conditions 16

II.4 Film Characterization 17

II.4.1 RHEED 18

II.4.2 Van der Pauw-Hall 21

II.4.3 X-ray Diffraction 22

II.4.4 Photoluminescence 25

II.5 Statistical Design of Experiment for PL Response 28

II.5.1 Independent Variables 29

II.5.2 Define Objectives/Design Experiment 29

II.5.3 Running the Experiment 30

III. EXPERIMENTAL RESULTS 32

III.1 Optomization of $Ga_{0.8}In_{0.2}N$ 32

III.2 Variation of Indium Content 34

III.3 Temperature Dependence of Luminescence 37

III.3.1 Variation of Luminescence Intensity with Temperature 37

III.3.2 Variation of the Bandgap with Temperature of $Ga_{0.8}In_{0.2}N$ 40

IV SUMMARY 42

IV.1 DOE 42

IV.2 Variation of Indium Content 43

IV.3 Recomendations for Future Work 44

REFERENCES 46

ACKNOWLEDGEMENTS 49

APPENDIX A: PHOTOLUMINESCENCE 50

APPENDIX B: ECR-MBE DESIGN AND ANALYSIS 61

APPENDIX C: STATISTICAL DESIGN OF EXPERIMENT 74

APPEDNIX D: X-RAY DIFFRACTION 81

I. INTRODUCTION

I.1 Project Description

The goal of this research project was to systematically explore the properties of III-V nitride thin films made with varying indium content. Specifically, we chose to look at (Ga,In)N, a alloy system with a direct bandgap for all compositions. The band gap energy can be varied from 1.89 (pure InN) to 3.47 eV (pure GaN). (Ga,In)N has potential applications for use in optoelectronic devices operating in the violet, blue and blue-green regions of the optical spectrum. Although showing considerable potential promise, the (Ga,In)N system has received relatively little prior study to determine how growth conditions affect the optical and electrical properties of the material. The study of indium and its roll in III-V nitride thin films is presented in this research and addresses these issues.

The epitaxial growth and characterization of III-V nitrides some additions to our laboratory. Our first task was to determine a suitable source for atomic nitrogen in the film growth. Here we chose electron cyclotron resonance plasma assisted molecular beam epitaxy (ECR-MBE). Our Perkin-Elmer MBE system was modified by inserting a commercially available ECR electromagnetic coil, made by AsTex Inc., into one of the source flanges. In addition to the ECR hardware, we also designed and built the gas-handling system to provide ultra-high purity nitrogen to the source.

Our next task was to develop a suitable characterization scheme. For our purposes, single crystal (Ga,In)N films are best characterized by using techniques such as *in-situ* reflection high energy electron diffraction (RHEED) and Van Der Pauw-Hall measurements which are readily available in our laboratory. They are both standard measurement techniques and are both quick and easy methods of semiconductor characterization.

X-ray diffraction (XRD) and photoluminescence spectroscopy (PL) are also widely used measurement tools. X-ray diffraction provides information on the microstructure of the

grown films. X-ray diffraction measurements on several of our samples were performed at the University of California at Santa Barbara and Northwestern University in Chicago. X-ray diffraction θ-2θ scans were performed in Ames Laboratory. Finally, there was no suitable PL setup on campus for wide bandgap semiconductors so a PL system was designed and constructed.

The next step in this study was to develop a growth process which would optimize the conditions necessary to produce the best quality III-V nitride thin films based on feedback from our characterization scheme. The addition of the ECR to the MBE system complicates the growth process by introducing several control variables which directly affect growth kinetics. The gaseous species from the plasma discharge is generally energetic and ion bombardment effects on the epilayer surface can become significant. Not only are substrate temperature and growth rate important factors in this process, but with the ECR, magnetic confinement, microwave power as well as the flow of nitrogen all become key parameters in the growth process.

With the wide range of controls in this growth process, it was determined that a statistical design of experiment (DOE) approach to system optimization would be most practical and efficient. This method employs a commercially available software package by ECHIP Inc. In this process we determine the most optimal control settings which produce the most desired responses from our feedback characterization measurements. For example, it was desirable to maximize the bandgap PL peaks while simultaneously minimizing any inherent sub-bandgap peaks. Early reports[1] have attributed sub-bandgap PL peaks to impurity and defect states. Samples exhibiting large PL peaks related to band-to band transitions while simultaneously minimizing midgap related peaks would suggest higher quality single crystal films for optoelectronic applications.

We then grew and characterized several $Ga_xIn_{1-x}N$ samples with x ranging from 0.9 to 0.1 in increments of 0.1. Growth parameters for these samples were based on the information

gained in the DOE. And finally we conducted temperature-dependent PL measurements in order to determine carrier activation energy as well as determine the exciton energy shift with temperature. Our results showed that our ECR-MBE system could produce good quality material with x ranging from 0.9 to about 0.4, well into the green portion of the visible light spectrum.

Our $Ga_xIn_{1-x}N$ films were n-type as determined by Van der Pauw-Hall measurements with carrier concentrations ranging from $5x10^{17}$ to $7x10^{18}$ cm^{-3} and mobilities decreasing from 175 $cm^2/V{\cdot}s$ to <10 $cm^2/V{\cdot}s$ with increasing mole fractions of In. As the indium content increased, the PL band edge peaks became less intense and shifted toward longer wavelengths. Also, θ-2θ XRD peaks shifted toward smaller angles corresponding to a larger lattice constant. These peaks again decreased in intensity. Indium-rich samples with $x<0.4$ were highly resistive and transport measurements were inconclusive which is characteristic of highly defective material. No PL was observed in these samples and θ-2θ XRD peaks were broad and noisy, again, suggesting poor quality material. These results invite further DOE system optimization for In-rich (Ga,In)N film growth. However, the scope of this study was limited to the blue and blue-green portion of the light spectrum as this technology is dominated by other optoelectronic materials operating at longer wavelengths which is far more developed than III-V nitride technology is at this point.

In summary, this work has progressed in four consecutive stages:

- system design and installation
- development of a suitable characterization scheme
- growth process development and optimization
- investigation of (Ga,In)N with varying indium content.

I.2 Important Properties of III-V Nitrides

I.2.1 Refractory Nitrides

The III-V refractory nitride solid solutions, indium nitride (InN), gallium nitride (GaN), and aluminum nitride (AlN), and their subsequent heterostructures are of considerable interest due, in part, to their unique electronic, optical, and mechanical properties. They are direct band gap semiconductors exhibiting high thermal stability with energy gaps in the spectral region ranging from 1.89 eV (InN), and 3.4 eV (GaN) to 6.28 eV (AlN).[1] Consequently, these materials are of interest for applications in short-wavelength light emitters and high energy photon detection systems, as well as devices for high-power and high-temperature electronics. Lattice constants and band gap energies for the wurtzite and zinc blend phases of the III-V nitrides are listed in Tables I.1 and I.2.[1]

Table I.1: Properties of wurtzite phase III-V nitrides.

Material	c (Å)	a (Å)	E_g (eV)
AlN	4.982	3.112	6.28
GaN	5.185	3.189	3.4
InN	5.760	3.548	1.89

Table I.2: Properties of zinc blend phase III-V nitrides

Material	a_0 (Å)	E_g (eV)
AlN	4.33	5.11
GaN	4.54	3.45
InN	4.98	2.2

Gallium nitride is important because of its band gap makes it a candidate for making light emitters in the ultra-violet (UV) region. Through alloying or by introduction of radiative mid-gap centers, GaN might also be extended for use in the blue and violet regions of the spectrum. GaN is also predicted to have a high ballistic electron drift velocity suitable for high-frequency and microwave devices.[2,3]

Aluminum nitride is an insulator and is a promising thin-film piezoelectric material with high acoustic wave velocity and a large piezoelectric coupling coefficient.[4] AlN and (Al,Ga)N alloys may be used in forming heterojunctions to make quantum well devices for optoelectronic devices.

Indium nitride, exhibiting the smallest band-gap of the III-V nitrides, provides a potential means for tailoring the optical properties of these materials into the blue and, possibly, even into the orange spectral region. InN is the least-studied III-V nitride due to past difficulties in growing good-quality crystals. The availabilty of more easily fabricated materials (most notably AlGaInP) that can be used for devices operating in the yellow and orange region of the spectrum has limited the attention to InN. However, band structure calculations[5,6] indicate a direct band gap and low electron effective mass, predict the potential for high speed photonic devices. Furthermore, as the only member of the group III-V nitride family with a band edge in the visible regime, InN is a natural choice for visible light photonic devices based on alloys with other, wider bandgap group III nitrides.

Ternary alloys composed of (Ga,In)N and (Al,In)N have been grown by various techniques.[5,6,7,8] These reports indicate stable growth of both alloys and confirm miscibility of solid solutions across the entire compositional range. However, no complete electrical or optical characterization has been presented on these materials. In this study we focus on the optical characteristics of the (Ga,In)N alloy system which is well suited for short wavelength visible light optical devices.[1]

I.2.2 III-V Nitride Phases

III-V nitrides exist in two polymorphs: Wurtzite and Zincblende.[1] The metastable Zincblende structure has a cubic unit cell, containing four of each type of atom. The Zincblende crystal structure is commonly observed in other III-V compounds such as GaAs, InP and AlSb. However, the Zincblende phase is not as common in III-V nitrides (and none were observed in our films grown for this work). In order to obtain cubic GaN, one must a suitable cubic substrate and the growth conditions must be carefully controlled. Even then, the resulting material is generally of poor quality. The Wurtzite crystal structure, on the other hand, is commonly observed in III-V nitrides. This structure has a hexagonal unit cell characterized by two lattice constants, c and a. It contains 6 atoms of each type. The Wurtzite structure consists of two interpenetrating hexagonal closed packed (HCP) sublattices, each with one type of atom, offset along the c-axis by 5/8 of the cell height (5/8 c).[9] The Wurtzite structure is shown in Figure I-1.

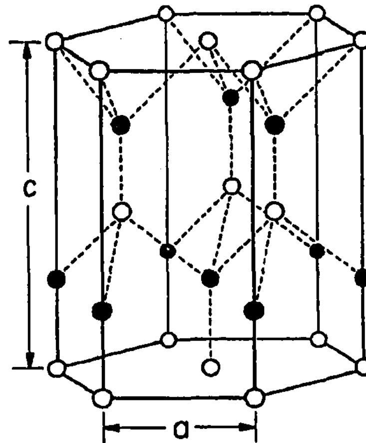

Figure I-1: The Wurtzite crystal structure. (reprinted from ref. 9)

I.3 Previous Work

I.3.1 Gallium Nitride

Gallium nitride, the most comprehensively studied of the nitride binaries, has been grown in both Zincblende and Wurtzite phases depending on the starting substrate and the growth conditions.[10] Bulk GaN substrates are not available and thus films must be grown heteroepitaxially on foreign substrates. Epitaxial stabilization of Zincblende GaN (β-GaN) thin films has been achieved on a number of substrates, including β-SiC,[11] GaAs,[12] MgO,[13] and Si.[14] Wurtzite phase films have been grown on both (0001) sapphire and α-SiC. Recently the discovery that AlN and GaN buffer layers grown at low temperatures (less than 500°C) play an important role in epitaxial growth has led to α-GaN films on GaAs and Si substrates.[15,16]

Single crystal III-V nitride thin films have been successfully grown by a number of techniques, including chemical vapor deposition (CVD),[17] metal organic chemical vapor deposition (MOCVD),[18] and molecular beam epitaxy (MBE).[19] All of these growth techniques produce films with high electron concentration, typically greater than 10^{17} cm^{-3}.. Most workers in this field agree that the high *n*-type carrier concentration is attributed to nitrogen vacancies because nitrogen incorporation probabilities are low.[2] Thus early failures at *p*-type doping were attributed largely to compensation by n-type defects. Recently, however, several modifications to MBE growth have been implemented to reduce growth temperatures by the incorporation of plasma assisted methods including, electron cyclotron resonance (ECR)[20] and reactive ion assisted growth (RI).[2] These low temperature growth techniques have successfully produced single crystal semi-insulating GaN films. The improvements in nitride film quality have subsequently led to recent reports on *p*-type GaN using column II elements such as Mg, Zn and Cd,[21,22,23] suggesting the possibility of fabricating efficient light-detecting and emitting devices.

I.3.2 Indium containing III-V nitrides

Indium nitride, on the other hand, has not received the attention given to GaN, primarily because the 1.89 eV band gap of InN corresponds to a portion of the electromagnetic spectrum in which alternative and more advanced semiconductor technology is available. However, since many device applications require wavelengths in the visible light spectrum, InN will find use in making ternary alloys with GaN and AlN, leading to lower gap semiconductors. Although indium-containing semiconductors (like GaInAs and GaInAsP) have been extensively developed for use electronic and optoelectronic applications, the full potential of indium-containing III-nitrides has not been fully explored. Indeed, reports on the growth and properties of (Ga,In)N alloys has been sketchy.

InN suffers from the same lack of suitable substrate material and high native defect concentration that have hindered progress in GaN and AlN. InN also has poor thermal stability[1] and cannot be grown at the high temperatures required by the various CVD growth processes which dominate in producing the best quality III-V nitrides to date.[23,24] Other workers have cited the large disparity of the atomic radii of In and N as a possible contributing factor to the difficulty in obtaining good quality InN. However, most (if not all) of the studies of InN and the related ternary III-nitride alloys have been done on CVD grown material.[1] To the best of the author's knowledge, there has been no extensive material characterization reported on ECR-MBE grown indium-containing III-V nitride alloys.

I.3.3 Devices

There have been scattered reports of devices fabricated from III-V nitrides. Most of these devices have been grown on α-SiC or (0001) Al_2O_3 substrates using either MOCVD or more recently, ECR-MBE. The most important commercial application of the wide-bandgap semiconductors is for visible light emitters in the blue, blue-green, and green spectral regions. In 1971, Pankove et al. fabricated the first blue-emitting "n-i-n" junctions in heteroepitaxial

GaN/Al_2O_3 films grown by VPE.[22] However, continued failures at device quality films produced in the 1970's and early 1980's had diminished the interest in these materials.[1] Recently, due to improved crystal growth techniques, excitement over the III-V nitrides has again soared in the last five years.

In March of 1994 Nakamura et al. demonstrated high-performance blue LEDs grown by MOCVD.[23] The LEDs were (InGa)N/(AlGa)N double heterostructures using Zn doped (In,Ga)N in the active layer. The typical output power was 1500 μW and the external quantum efficiency was as high as 2.7% at a foreword current of 20 mA. These LEDs represent the first known commercial introduction of optoelectronic devices based on III-V nitrides.

Recently, Molnar *et al.* at Boston University, reported blue emitting LEDs grown by ECR-MBE without the need for any post-process annealing to activate the Mg acceptors in the *p*-layer.[24] The devices began to emit light with an applied bias of 3 volts and had spectral emission peaks at 430 nm. Devices with improved geometries as well as etched mesas are currently under development and are expected to show improved characteristics.

High density optical recording, in particular, is a commercially important application for injection lasers fabricated from III-V nitride alloys. Degradation at high current densities in II-VI based blue-green light emitters has turned the research community toward the nitrides as a possible alternative material system.[25] For example, II-VI ZnSe based blue-green lasers operate for only for a few minutes to an hour at room temperature before breaking down, while II-VI LEDs function from a few tens of minutes to a few days before burning out.[26] Early studies demonstrate that III-V nitrides are very robust and remain stable under adverse thermal conditions.[27] These materials not only display mechanical stability under extreme environmental conditions, but the energy bandgap has a very small temperature dependence compared to other III-V materials. Measurements by Guo et. al. show that the variation in band gap increases in the order of N, P, and As for the column V element.[28]

No GaN lasers have yet been reported. However, stimulated emission from optically

pumped III-V nitride heterostructures grown by MOCVD has been observed by several groups.[29,30,31] Khan *et al.* reported room temperature violet (415 nm) stimulated emission in the vertical cavity mode from photo-pumped GaN/(In,Ga)N heterostructures,[29] as indicated by a clear narrowing of the width of the spectral peak at threshold. With the rapidly developing methods of nitride fabrication, room-temperature injection laser operation is certainly on the horizon.

A variety of other III-V nitride devices has also been reported. Ultraviolet detectors based on gallium nitride have been reported with high responsivity between 200 and 362 nm with a sharp wavelength cutoff at 362 nm.[32] These photoconductive detectors exhibit gains of over 85dB. These detectors can be utilized in the development of a focal plane array for UV imaging.

In 1993, Khan *et al.* reported the fabrication and dc characterization of a GaN high-electron-mobility transistor (HEMT).[33] A HEMT with a 4 μm gate length showed a transconductance of 28 mS/mm at 300 K and 46 mS/mm at 77 K. Complete pinchoff was observed at a gate bias of −6V.

In addition to the devices described above, there have been demonstrations of high-reflectivity distributed Bragg mirrors[33], quantum-size effects in AlGaN/GaN quantum wells[33], and negative electron affinity in AlN heterostructures.[34] While interest is currently focused on the optoelectronic properties of the III-V nitrides, they also appear to be poised to expand the operational envelope of high-performance electronic circuits as well.

I.4 Potential Applications

The broad range of device applications for wide-bandgap semiconductors has placed the III-V nitride material system as a prime candidate for optoelectronic research. The blue and UV wavelengths are a technologically important region of the electromagnetic spectrum in which progress in semiconductor development is a high priority. At present, semiconductor

devices operate routinely from the IR to green wavelengths. Extending this range into the blue region would permit semiconductor devices to emit and detect the three primary colors of the visible spectrum. This would have a significant impact on imaging and graphic applications.[1]

Another important region of the electromagnetic spectrum occurs in the 240-280 nm range. Absorption by the ozone makes the Earth's atmosphere nearly opaque to detection and emission in this region. Space-to-space communications in this band would be secure from Earth , yet vulnerable to satellite surveillance. The nitrides are also expected to exhibit superior radiation hardness compared to GaAs and Si, which also makes them attractive for space applications.[1]

Traffic lights may prove to be yet another fertile application for blue-green LEDs. Total power consumption by traffic lights reaches into the GW range. GaInN/AlGaN blue-green LED-based traffic lights, with an expected electrical power consumption 12% that of present incandescent bulb traffic lights, promise to save vast amounts of energy. LEDs emit blue-green, red and yellow colors themselves without the use of color filters such as those found in white bulb traffic lights. Employing these high-brightness blue-green LEDs can lead to safe, energy-saving roadway and railway signals in the near future based on III-V nitride materials.[21]

Short wavelength emitters and detectors have potential applications in data storage systems as well. The amount of memory of a data storage system is limited, in part, by the wavelength of the driving devices. Digital information storage density can be increased quadratically with decreasing wavelength. It is estimated that information at a density approaching 1 Gbit cm^{-2} should be possible using blue light to write and detect data.

The potential device applications for the III-V nitrides are very broad, including UV and visible LED's and injection lasers, photodetectors, photocathodes, high temperature electronics, and low power electronics. It can be expected that these materials will become very.important commercially before the end of this decade.

II. EXPERIMENTAL

In this section are described the experimental tools developed for growing and characterizing nitride layers. Once the MBE system had been modified to a source of nitrogen, and the basic characterization tools had been put in place (primarily photoluminescence), we spent some time growing layers of pure GaN. We did this to become familiar with the operation of the ECR source in our MBE system, and to "tune" the characterization tools. Once we confident that we could grow GaN that had properties similar to what had been reported in the literature, we then turned our attention to optimization of the growth of (Ga,In)N. A major part of that development was the use of the design of experiments (DOE) technique.

II.1 ECR-MBE

The III-V nitride films in this experiment were grown in a Perkin-Elmer 430 MBE system modified by the addition of an ECR plasma source (AsTex Compact ECR) which was inserted into the number eight effusion cell port of the MBE source flange. The deposition system is schematically illustrated in Figure II-1. This plasma source is designed for use in plasma enhanced chemical vapor deposition, plasma etching, surface cleaning, and molecular beam epitaxy.

The ECR-MBE system offers several features which are compatible with low-temperature, ultra-high-vacuum thin-film growth. ECR is a method of producing a dense plasma at low pressures which provides atomic nitrogen required for epitaxial growth. Due to the large mean free path of the gaseous species at these low background pressures (about 1 meter at 10^{-4} Torr), the growth is carried out in the molecular flow regime. This is where the transport of atoms or molecules in both thermal beams from the MBE effusion cells as well as the beam of activated nitrogen from the ECR source occur in a collisionless manner. Also, the

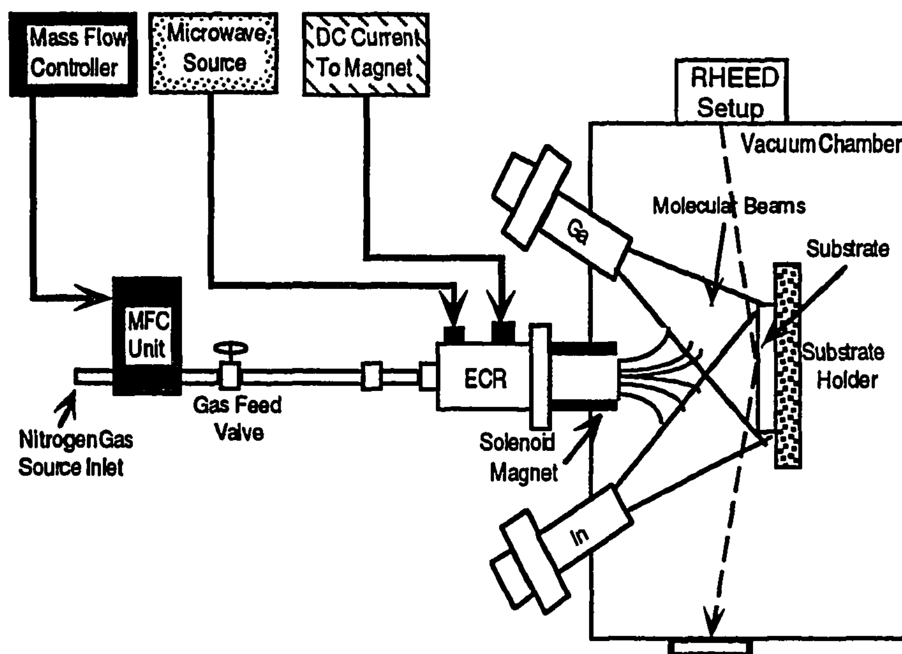

Figure II-1: Schematic representation of ECR-MBE setup

ECR-MBE growth process involves no other species except gallium, indium and activated nitrogen in the growth chamber, thereby reducing potential impurity contamination.

The method by which the ECR source produces an atomic nitrogen beam is fairly simple. High-purity nitrogen gas passes through a metallic cylindrical waveguide, which sits along the axis of an electromagnet coil. Current flowing in the coil winding induces an axial magnetic field, which in turn causes any charged particles (electrons or ions) passing down the waveguide to rotate in a cyclotron motion. The circular motion of the charged particles greatly increases their total path length as they move down the waveguide, and thus greatly increases the probability of collisions with neutral molecules and atoms in the flowing gas stream. In addition to the DC magnetic field, microwaves are launched down the waveguide in the same direction as the gas flow. In general, the electromagnetic waves will consist of some combination of right- and left-circularly polarized (RCP and LCP) traveling waves. The RCP waves match the direction of rotation of electrons in the magnetic field. At some point along

the ECR waveguide, the cyclotron frequency of the rotating electrons matches the frequency of the traveling electromagnetic waves. This resonance is known as the ECR condition. At the point where the ECR condition holds, the rotating electrons will be accelerated by the microwave field. On collision with neutral nitrogen molecules, the high energy electrons can break apart (crack) the molecules, creating a stream of nitrogen atoms (both ionized and neutral) which flow out of the ECR source towards the substrate. It is the atomic nitrogen that incorporates into the growing GaN film.

Because the magnetic field can be varied, the point at which the ECR condition occurs can be moved up and down the axis of the waveguide. (See Appendix B for a more complete description of the spatial dependence of the magnetic field.) As we will see, this variation of the ECR point will play an important role in the optimization of the growth of (Ga,In)N.

In practice, approximately 10% of the molecular nitrogen gas is converted into atomic nitrogen. In order to maintain a stable plasma, the pressure inside the ECR waveguide needs to be on the order of 10^{-3} Torr. This high pressure is not particularly compatible with the normally ultra-low pressure environment in the MBE growth chamber. A thin boron nitrides disk with a small aperture ($\approx$ 1 cm diameter) at the exit of the ECR waveguide helps maintain higher pressure in the ECR source itself. Even so, the pressure in the MBE growth chamber can climb into the 10^{-4} Torr range during the operation of the ECR source. This high pressure stresses the pumps and components of the MBE system, which was designed for operation in the the 10^{-7} Torr range.

The peripheral supporting electronics for the ECR plasma source consist of an AsTex S-250 microwave power generator coupled to the ECR source by a flexible cylindrical wave guide approximately 0.75" in diameter. Microwave power transfer is optimized by a coaxial slug tuner. Microwave power can be varied from 0 to 250 watts. An AsTex EMS 40-25 power supply is used to supply current to the magnet coil. The current supply varies from 0 to 20 Amps. The process gas is ultra-high purity nitrogen introduced to the ECR source through

a mass flow controller (Unit Instruments model UFC 1100). The mass flow can be varied from 0 to 50 sccm.

Conventional Knudsen effusion cells are used to evaporate Ga and In. The base pressure in the overall system is typically 10^{-10} Torr. A reflection high energy electron diffraction (RHEED) provides *in situ* characterization of the film growth. RHEED consists of a beam of electrons directed at a low angle (1-3°) to the sample surface. The defracted electron form a pattern on a fluorescent screen on the opposite side of the MBE growth chamber. For diffraction from atomically smooth surfaces, the RHEED pattern usually consists of elongated streaks which are normal to the shadow edge on the screen. The surface temperature of the growing film is measured with an optical pyrometer. A thermocouple mounted on the heater station behind the sample mounting block served to control the substrate temperature.

II.2 Sample Preparation

Our initial III-V nitride films were grown on both Si (100) and GaAs (100) substrates. However these substrates produced poor quality films. Numerous other researchers also reported that films grown on Si and GaAs substrates were of poor quality and displayed poor optical properties.[1,2,4,7] All of the samples discussed in this dissertation were grown on (0001)-oriented Al_2O_3 (sapphire), obtained from Union Carbide.

Before growth, the sapphire substrates were degreased using a sequence of boiling TCA, acetone, and methanol. Following the degreasing procedure, the substrates were etched for 5 minutes in hot H_3PO_4:H_2SO_4 (1:3) to remove surface contaminants and mechanical damage due to polishing. After these steps the substrates were rinsed in de-ionized water, spin-dried and mounted on molybdemun blocks, and loaded into the introduction chamber of the MBE system.

It was discovered that blocks using conventional indium bonding could not be

heated high enough to fully desorb the substrate surface. Also, these growths typically lasted several hours at high temperatures, and the indium used for bonding tended to evaporate and react with the film during the growth. For this reason, special blocks were designed to hold one quarter wafers as well as whole wafers. These "non-bonded" blocks were designed to allow more efficient heating the samples.

The wafers were pre-baked for approximately one-half hour at 850°C in the preparation chamber and then transferred into the main growth chamber where they were subjected to nitrogen bombardment for another half hour at 850°C. This "nitridation" step produces a thin layer of AlN as the N atoms react with the Al atoms at the surface of the substrate.[9]

II.3 Growth Conditions

There are several key parameters comprising the growth conditions which determine the structure and the microstructure of the III-V nitride films grown in this experiment. To begin with, there are a wide range of substrate materials from which to choose, as described in the first chapter. Here we have chosen sapphire (Al_2O_3) which is closely lattice matched to the III-V nitride family as well as affordable. However the mismatch is still on the order of 15% and strain plays an important role in crystal structure. The substrate temperature during the growth also affects growth kinetics. This primarily determines the surface mobility of the adatoms and re-evaporation of In becomes a problem at higher temperatures.[16] The growth rate is also a crucial parameter because when the rate is too high, nitrogen incorporation becomes incomplete and the growth is non-stoichiometric.[36] When the growth rate is too low, the process is too time consuming to be of any commercial value. Another important factor is the buffer layer which is grown at low temperatures during nucleation. The buffer layer accommodates the lattice mismatch between the substrate and the epilayer and decreases the dislocation density.[37]

With the inclusion of the ECR in the growth process, several key control parameters

were also addressed and analyzed. The microwave power, which energizes the ECR process, determines the kinetic energy of the nitrogen ions at the substrate surface. High ion energies can induce damage to the epilayer surface. The current to the electromagnetic coil controls the proximity of the ECR process relative to the substrate, again affecting surface damage. And finally, the nitrogen mass flow must be sufficient in order to maintain a stable plasma discharge as well as to accommodate stoichiometric growth.

II.4 Film Characterization

The purpose of these experiments is to determine suitable growth conditions which facilitate optimization of the quality of these materials for optical and electronic purposes. Furthermore, characterization techniques have been chosen which best determine the structure of the films thus providing a feedback mechanism for subsequent growths. Finally, the information gained in these experiments is utilized to determine reasonable windows of operation for each control variable and, more importantly, which parameters affect the film quality.

In this section, our initial growth strategies of GaN, AlN, and (Ga,In)N by electron cyclotron resonance plasma-assisted molecular beam epitaxy are reviewed. Particular emphasis is placed on the growth of these materials in two temperature steps. In the first step, a low-temperature (≤450°C) buffer layer, typically 200-800Å, is grown. This layer is usually polycrystalline. In the second step, the substrate temperature is raised to 500-800°C, for the duration of the film growth. This layer is usually single crystalline.

Emphasis on these growths was put on the growth rates and the specific substrate temperature during the bulk of the growth of the main film. Also, the ECR microwave power setting ranged between 20 and 100 W and the nitrogen flow was purposely kept low, typically between 10 and 20 sccm. Table II-1 lists all of the growth conditions of the films grown on sapphire.

Table II-1: Growth conditions for GaN films grown on Al_2O_3

Sample	Buffer Layer			Film		ECR		
	Material	Temp (°C)	G R (μm/hr)	Temp (°C)	G R (μm/hr)	I_B (A)	MWP (Watts)	MFC (sccm)
9409-4	GaN	450	0.2	600	0.2	18	35	20
9409-10	GaN	450	0.2	700	0.2	15	30	15
9409-12	GaN	500	0.2	700	0.2	14	35	15
9409-13	GaN	650	0.2	650	0.25	16	62	20
9410-2	GaN	650	0.25	690	0.25	17	45	20
9410-4	GaN	650	0.25	722	0.25	16	35	20
9410-5	GaN	750	0.25	700	0.1	15	35	20
9410-7	AlN	750	0.15	700	0.15	18	100	20
9411-2	GaN	600	0.1	600	0.2	17	75	15
9411-3	AlN	450	0.1	650	0.2	16	35	15
9411-7	AlN	450	0.1	800	0.2	13	35	20
9411-10	AlN	450	0.1	700	0.2	18	45	15
9501-1	AlN	780	0.423	780	0.4	13	20	10
9502-3	AlN	525	0.2	750	0.25	15	20	10
9502-4	GaN	450	0.25	750	0.2	18	20	10

The structure and microstructure of selected films were studied by the following characterization methods:

- Reflection High Energy Electron Diffraction (RHEED),
- Van der Pauw Hall Measurements,
- X-Ray Diffraction (XRD), and
- Photoluminescence (PL).

II.4.1 RHEED

In situ RHEED observation of the growth process in the MBE provides first-hand feedback for the initial nucleation of the III-V nitride film and also is a method of monitoring the progress of the film during growth. This helps in choosing the substrate

temperature as well as setting the relative fluxes of the source materials. However, RHEED only gives qualitative information about the microstructure of the film, and *ex-situ* characterization measurements, like X-ray diffraction, are used to further evaluate material quality.

Figure II-2 shows a RHEED pattern of the c-plane sapphire substrate after exposure to the nitrogen plasma. When sapphire substrates are first put into the growth chamber, the RHEED pattern from the substrate surface is diffuse, meaning that there is no distinct RHEED pattern. After exposure to nitrogen, the surface smooths and the RHEED becomes streaky. Presumably, a thin layer of AlN has formed at the due to the nitrogen exposure.[20] The streakiness of the diffraction patterns suggest that the AlN layers are atomically smooth. The spacing between RHEED lines is consistent with a surface layer of AlN. The lattice constant at the surface is 3.1Å, which is the in-plane lattice constant of Wurtzite AlN. The lattice constant was determined using the diffraction equation[38]

$$Rd = C\lambda \qquad \text{(II-1)}$$

where R is the measured distance between diffraction lines on the RHEED screen, d is the interatomic spacing, λ is the incident electron beam DeBroglie wavelength, and C is the camera constant of the RHEED set-up. The product $C\lambda$ for our system was determined previously using during GaAs layer growths.

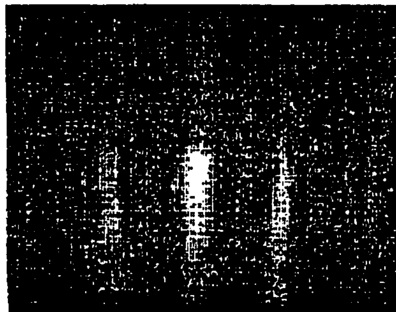

Figure II-2: RHEED pattern after 30 minutes of nitridation of the sapphire substrate.

After nitridation of the substrate surface, a thin (≤800Å) GaN or AlN buffer layer was deposited on the substrate at low temperatures, typically 450°C. Figure II-3 shows a typical RHEED pattern during the buffer layer growth. The streakiness of the patterns from these buffer layers on the sapphire substrates suggest that the epilayers are single crystal and atomically smooth.

Following the low-temperature buffer layer, the substrate temperature was raised to the desired growth temperature and the GaN "active" layer was grown. Typical growth rates for the active layer were between 0.1 μm/hr and 0.2 μm/hr. (Note that these GaN growth rates are much lower than typically used for other types of III-V MBE growth, a result a the relatively low flus of activated nitrogen.) Typically, a total of one micron of GaN was grown in these preliminary samples.

Figure II-4 shows a typical RHEED pattern of the GaN films during growth. These reveal the same epitaxial relationship between GaN films and the substrate as the corresponding GaN and AlN buffer layers. Again, the films are well ordered and atomically smooth throughout the growth.

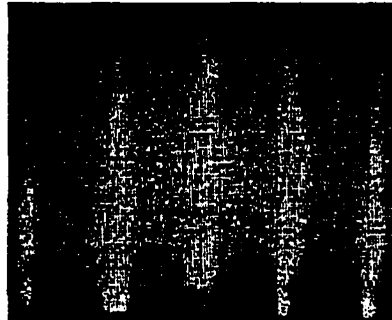

Figure II-3: Typical RHEED pattern after 12 minutes of buffer layer growth on sapphire.

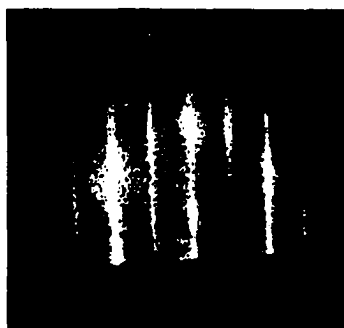

Figure II-4: RHEED pattern for GaN film after 1 hour of growth

II.4.2 Van der Pauw-Hall

In order to determine transport properties (carrier types, carrier concentrations, and carrier mobilities) Van der Pauw and Hall measurements were performed on samples following growth.[39] Typically, the grown films of GaN were n-type with carrier concentrations in the range of $10^{17} - 10^{18}$ cm^{-3}, results that are consistent with previous reports of GaN. In some cases our films were highly resistive. We interpreted such results to mean that those samples were of very poor quality. Samples for van der Pauw and Hall measurements were made by cleaving small squares (approximately 5 mm x 5 mm) from the grown samples and melting small In dots in the corners for electrical contacts.

Table II-2 shows the results of the some of the GaN samples that were grown and measured. Sample 9409-10 had the highest mobility (30 $cm^2/V{\cdot}s$) and the lowest *n*-type carrier concentration (3.3×10^{17} cm^{-3}) of all the GaN samples we grew. The ECR settings in conjunction with the substrate and the growth rate are crucial to obtaining these results.

Table II-2: Van der Pauw results and RHEED pattern description of selected samples grown on sapphire

Sample	Mobility ($cm^2/V\cdot s$)	Concentration (cm^{-3})	RHEED Description
9409-10	29.8	$3.3x10^{17}$	clear and streaky
9411-2	9.2	$5.1x10^{18}$	not clear and faded
9411-3	11.8	$3.8x10^{18}$	streaky
9411-10	14.8	$3.8x10^{18}$	streaky
9502-3	13.1	$2.4x10^{18}$	faded quickly
9502-4	4.3	$3.9x10^{18}$	streaky but faded

Sample 9409-10 had a 400 nm GaN buffer layer grown on a sapphire wafer that was exposed to the nitrogen plasma for 45 minutes. The substrate temperature during the buffer layer growth temperature was 450°C. The growth temperature of the subsequent GaN film was 700°C. The ECR had a microwave setting of 30 W foreword power and the mass flow of the nitrogen gas was 15 sccm. The growth rate was established at 2000 Å/hr. The RHEED pattern was exceptionally sharp for this particular growth.

II.4.3 X-ray diffraction

Two different types of X-ray diffraction techniques were used to evaluate our nitride layers. The first is the θ-2θ method which probes ordering normal to the substrate and depends on the Bragg condition for X-ray diffraction. The second is the rocking curve method in which the sample is "rocked" through the Bragg condition. The width of the resulting peak is related to the overall crystal quality. These two techniques are further discussed in Appendix D.

X-ray diffraction θ-2θ scans as well as rocking curves at the main reflection peak

were performed on selected samples. Figure II-5 shows a typical θ-2θ scan and rocking curve for a typical sample. The θ-2θ peaks can be indexed as the (0002) diffraction of GaN occurring at $2\theta = 34.6°$ and the second order harmonic occurring at $2\theta = 72°$. The samples included sample 9409-10 and others displaying similar characteristics.

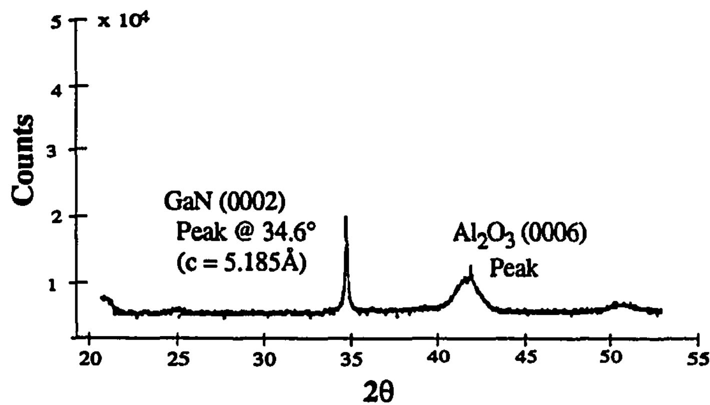

(a)

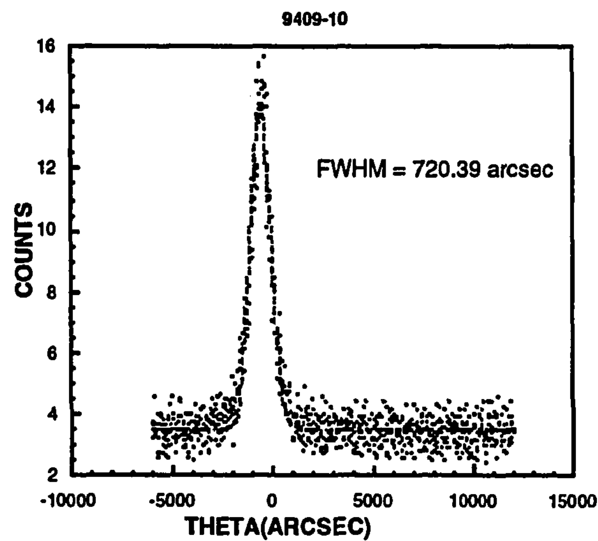

(b)

Figure II-5: X-ray diffraction measurements for GaN grown on sapphire (sample number 9409-10): a) θ-2θ scan and b) rocking curve.

The other samples were grown with slight variations in growth conditions in order to determine which parameters induce the greatest change in the film characteristics. The full width at half maximum of the XRD rocking curve data is given in Table II-3 for the selected samples.

Table II-3: XRD rocking curve data for selected films.

Sample	**FWHM** (arcmin)
9409-10	12
9411-02	22
9411-03	20
9411-10	21
9502-03	44
9502-04	19

While rocking curves are very useful for comparing crystalline quality of different samples, we were not able to use the rocking curve method for our (Ga,In)N samples. The was no easily accessible local diffraction set-up with accuracy sufficient to be useful in measuring our samples. The time lag involved in sending out samples to other laboratories was too great to be useful. So for the (Ga,In)N work our X-ray capabilities were limited to θ-2θ scans.

X-ray diffraction data, when used together with the RHEED and Hall data for the selected samples in this study, indicate that all the films are single crystalline and of fairly high quality with FWHM of XRD rocking curve ranging from 10-45 arc-min. The film quality was correlated with the microwave plasma power, magnet current, and substrate temperature during film growth. However, we did not grow enough of these GaN samples to pin down the correlations. Again, our goal was to focus on the alloy $Ga_{0.8}In_{0.2}N$.

II.4.4 Photoluminescence

Photoluminescence (PL) has been established as one of the most powerful and versatile techniques to investigate intrinsic as well as defect-related properties of semiconductor materials. PL provides information on the types of radiative transitions occurring in a sample. It is particularly useful for the detection of shallow-level impurities, but can also detect certain deep-level impurities, provided that radiative recombination events dominate non-radiative recombination. Because of its versatility, PL is the most important characterization tool in this research. PL peak position shifts as well as relative peak intensities help determine the effect of the various control parameters in the growth process as well as that of varying the indium mole concentration in the films. A detailed discussion on photoluminescence as well as the particulars of our experimental setup are presented in Appendix A.

One potential difficulty in comparing the peak intensities obtained from different samples is error in setting up the measurement. Excitation power, repetition rate, system noise, and beam focusing can all lead to "set-up" errors, which could lead to considerable variance in measured peak intensities and render them useless as comparative standards. Note that peak *locations* are less prone to set-up error since the locations of peaks do not depend on any of the above measurement settings. In order to insure the reliability in consecutive PL measurements, we conducted a series of measurements from a single GaN sample in an effort to develop a measurement procedure which would lead to reproducible results. We were able to develop a standard PL set-up which would give at most 7% variance on peak intensities obtained in separate measurements from a single sample. This gave us confidence needed in order to use peak intensities as a means of comparing different samples.

Figure II-6 shows typical PL spectra from a GaN film (again sample 9409-10) grown in our laboratory. The sample exhibits two characteristics commonly seen in

GaN.[42,43] First is strong band gap peak (probably recombination through a bound exciton) at 3.47 eV. The second feature is a weaker and much broader band of luminescence centered at 2.2 eV. This mid-gap luminescence band has been attributed to carbon contamination in the films or to ion damage induced during the growth process.[44]

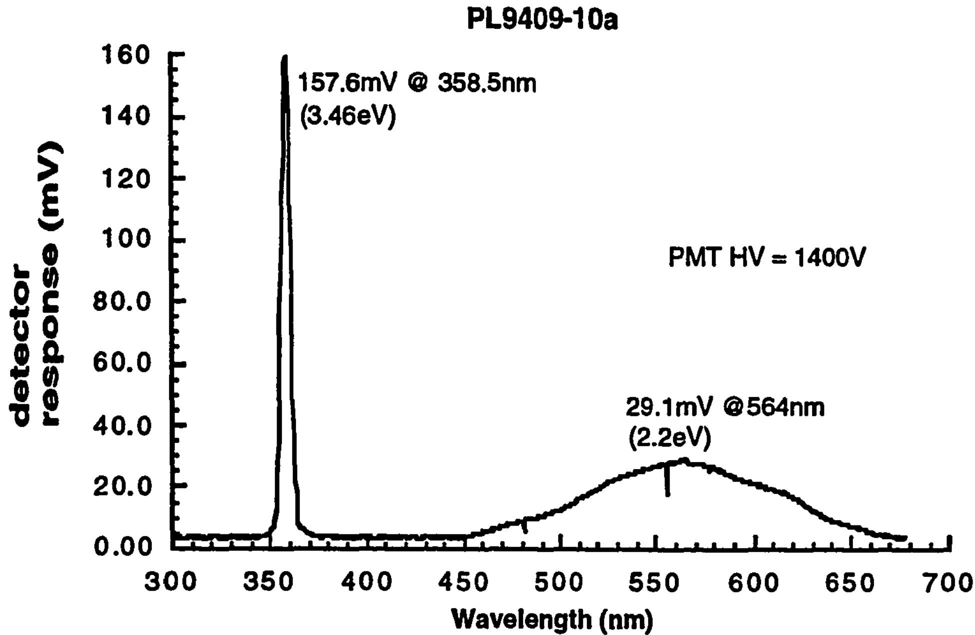

Figure II-6: Typical PL spectra of a GaN film.

Before starting on the optimization procedure, we grew a handful of (Ga,In)N films. The PL spectra of these layers were characterized by two midgap photoluminescence peaks at about 2.67 eV and 2.47 eV, in addition to the expected excitonic peak at around 3.1 eV for $Ga_{0.8}In_{0.2}N$. Figure II-7 shows a typical PL spectra of a $Ga_{0.8}In_{0.2}N$ film with the bandgap peak and two midgap peaks. Subsequent growths revealed that not only were the peak intensities affected by the growth conditions, but the relative intensities between the midgap peaks and the exciton peak were also affected by these parameters.

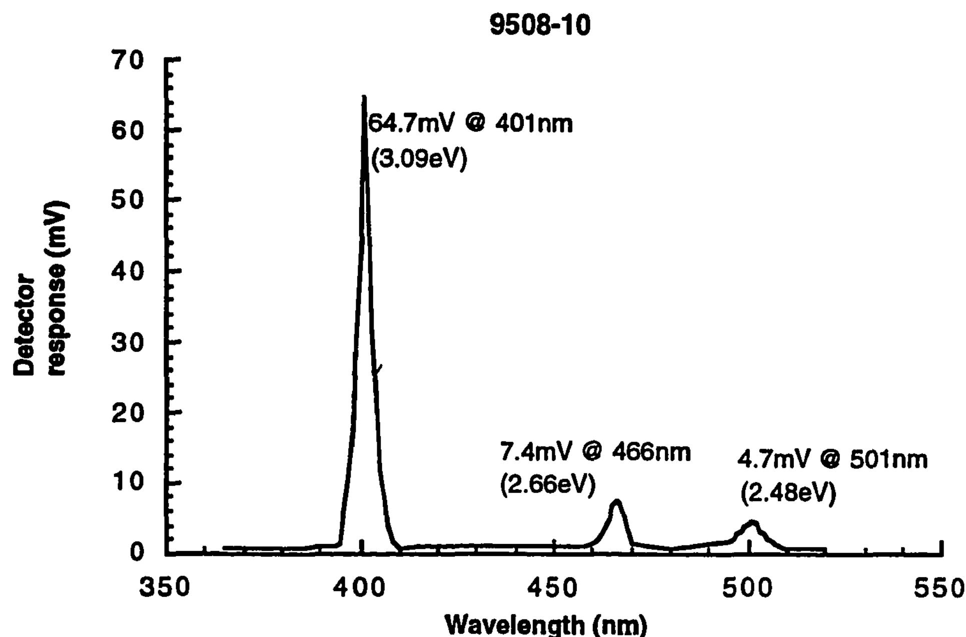

Figure II-7: PL spectra of (Ga,In)N film

From these preliminary growths of GaN, certain conclusions were evident about the limits of operation of the ECR and our MBE system. The parameters over which we had direct control were divided into two categories: 1) those which we felt were either optimized in our preliminary GaN growth or those offered very little latitude in how they could be set, and 2) those which we could vary and felt were likely to play a role in film quality. The growth parameters falling under the first condition are as follows:

- Mass flow — The ECR plasma was most stable when the mass flow was set at about 20 sccm. At lower flows, the plasma tended to be unstable (occasionally extinguishing itself). At high flows, the growth chamber pressure became too high.
- Buffer layer material — Buffer material choice did not seem to affect film quality, an observation supported by the literature.
- Buffer layer temperature — The substrate temperature during the buffer layer

growth did affect nucleation at the substrate/buffer layer interface. RHEED patterns during buffer layer growth were most clear and sharp when the substrate temperature was between 425°C and 450°C. This offered little room for variance, so we chose to keep this constant.

- Growth rate — The maximum growth rate achievable was about 0.2 μm/hr. Above this, the films were of poor quality. This growth rate is limited by the available flux of atomic nitrogen.

Parameters which we included as variables in the optimization process were:

- Magnet coil current — The magnetic field could only support a plasma when the current was set between 13 and 18 amps. These limits represent the range used in the DOE process.
- Microwave power — Strong evidence of ion damage appeared in samples grown with microwave power set above 100 watts. When the microwave power was below 20 watts, an insufficient nitrogen flux occurred and the growth was non-stoichiometric.
- The plasma was also most stable when the mass flow was at about 20 sccm. When the mass flow was above 20 sccm, the chamber pressure became too high and was not in the desired collisionless molecular flow regime.

II.5 Statistical Design of Experiment for PL Response

The combination of ECR with MBE leads to a classic multivariable growth process. The control parameters not only affect the film characteristics individually, but also interact and produce combined affects. For this reason, the traditional method of running experiments while varying one parameter and holding all others constant is time consuming and inefficient. Instead we have elected to use a statistical design of experiment (DOE) approach to optimizing the growth of (Ga,In)N. Here we employ the use of ECHIP, a software package designed for

this type of application. When implemented, the software asks for a list of all the control variables and their respective ranges. The program then suggests a series of experiments with various control settings. Finally, the feedback or response variables for each experiment are analyzed by the program. The program uses a mathematical model that predicts how input or control variables interact to create output variables or responses in a process or system. The following sections briefly describe how DOE relates to our plans to grow (Ga,In)N. The details of DOE are described in Appendix C.

II.5.1 Independent variables

As described in the previous chapter, the following key variables and practical ranges of operation were identified (Table II-4).An understanding of the effect of these variables is necessary to understand and interpret the results of the experiment.

- The buffer layer accommodates the lattice mismatch between the substrate and the nitride film
- The substrate temperature determines the surface mobility of the adatoms and their ability to occupy lattice sites. This is further complicated by the fact that high surface temperatures cause re-evaporation of indium, thus affecting the In/Ga ratio.
- ECR microwave power controls the amount of atomic nitrogen required for stoichiometric growth. However high microwave power promotes ion damage to the film surface.
- Finally, the ECR magnet current controls the position of the ECR condition relative to the substrate surface. This can also affect the amount of ion damage to the film.

II.5.2 Define objectives/design experiment

The objective then was to determine the effect of the growth conditions on the response variables. Once these relations were understood, one could decide what combination of control settings would minimize the midgap peaks and simultaneously maximize the exciton peak. This would insure that the photonic emissions would be dominated by band-to-band type transitions rather than with trap or defect related transitions and hence better crystal quality.

Table II-4: Key control variables for DOE

Control Variable	Minimum	Maximum
Buffer Layer Thickness	200 Å	800 Å
Substrate Temperature	450°C	600°C
ECR Microwave Power	25 W	85 W
ECR Magnet Current	13 A	18 A

II.5.3 Running the Experiment

As mentioned previously, minimum and maximum settings for each variable were based on experience. Middle settings were also selected for the center point. When the data for the settings of variables and decisions about the quadratic model with center points were entered into the system, the software called for a total of 25 trials. These trials consisted of 20 unique experimental runs with a repetition of 5 of these 20.

Repetition is a technique for statistically determining error. The settings for individual variables and the random sequence of the trials generated by the software is given in Table II-5, which shows the distribution of high and low settings for the 20 unique trials and the middle settings for the 4 center point replications. Each sample was grown according to these growth conditions. Each film was grown at a growth rate of 0.2 μm/hr for 5 hours for a total thickness of 1μm. Low temperature (<25K) PL measurements were performed on each sample. Also, Van der Pauw-hall and θ-2θ XRD were performed on selected samples.

Table II-5: Growth conditions for (Ga,In)N as chosen using the DOE approach.

Trial	Buff.Thickness(Å)	T_s(°C)	MWP(W)	I_B(A)
1	500	600	25	13
2	500	450	25	18
3	200	450	85	16
4	500	525	85	18
5	800	525	60	18
6	200	450	25	13
7	200	600	25	16
8	200	450	25	18
9	800	600	85	18
10	200	525	25	18
11	800	600	25	13
12	200	600	85	13
13	800	450	60	13
14	800	450	25	16
15	500	600	60	18
16	800	450	85	13
17	800	600	25	18
18	200	600	85	18
19	800	450	85	18
20	200	525	25	18

III. EXPERIMENTAL RESULTS

III.1 Optimization of $Ga_{0.8}In_{0.2}N$

Table III-1 shows the PL peak intensities of for the exciton and the two mid-gap levels for each of the 25 trials suggested by ECHIP. Again, trials 1-20 are unique trials and trials 21-25 are repetitions of the first five. After the data is entered into the system, the first consideration the model addresses is what variables have an effect on what responses.

Table III-1: PL results of DOE; PL response amplitude in mV.

Trial	Band Gap Peak	Mid-gap 1	Mid-gap 2
1	65.6	7.6	4.8
2	76.4	2.2	3.5
3	67.3	9.1	4.1
4	64.1	11.2	7.9
5	39.6	17.2	18.4
6	31.2	19.4	22.1
7	18.3	17.5	20.7
8	10.1	16.3	16.2
9	51.3	17.4	12.8
10	58.2	11.5	9.4
11	47.6	15.3	14.1
12	27.6	18.9	20.0
13	16.4	16.9	18.7
14	35.3	19.2	20.1
15	54.1	13.2	13.3
16	43.7	15.9	16.2
17	73.6	2.8	4.1
18	71.8	3.7	4.1
19	60.8	13.6	8.3
20	20.5	19.5	22.3
21	64.7	7.4	4.7
22	76.7	2.7	3.2
23	64.1	8.6	4.4
24	61.8	11.7	8.1
25	41.3	16.9	18.7

The key variables which had the most significant effect on the response variables were the current to the ECR magnetic coil and the power to the ECR microwave generator.

A key tool for detailed analysis of the experimental results is the contour plots generated by ECHIP. Each plot, which is presented in both two and three dimensions, provides a visualization of how these two variables interact at different settings (Figure III-1).

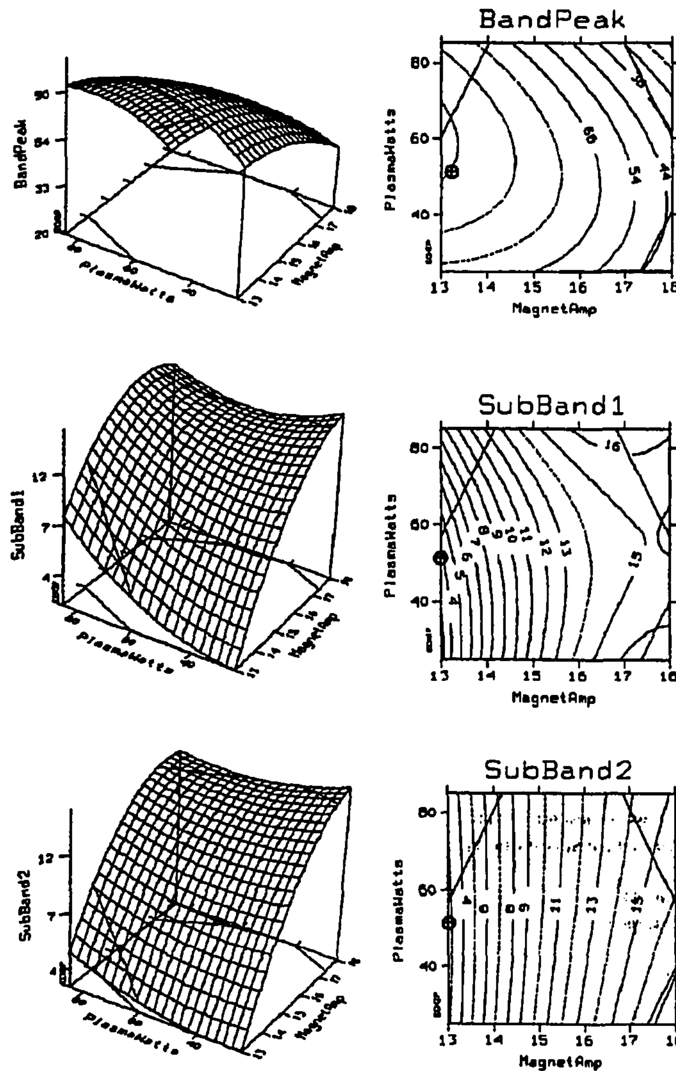

Figure III-1: Response surfaces in 3D and contour plots.

ECHIP is capable of showing any combination of control variables and their combined effect on the response variables. It is also capable of determining the combined effect of all four control variables and thus predicting an optimal setting scheme for the entire system which would produce the best quality (Ga,In)N single crystal thin films. The predicted optimal settings were as follows:

- Buffer layer thickness = 600Å
- Substrate Temperature = 600°C
- ECR Microwave Power = 40 W
- ECR magnet Current = 13 A

We decided to challenge the predictions suggested by ECHIP by growing three samples at or near these settings and comparing the results. The settings and results are presented in Table III-2.

Table III-2: Results of optimized control settings

Trial	Buff	T_s	MWP	I_B	Band Peak	Mid-gap 1	Mid-gap 2
1	590	600	40	14	71.3	4.7	2.1
2	600	590	35	13	96.2	3.6	2.4
3	600	600	40	13	97.1	3.4	2.3

Van der Pauw-Hall measurements on these films yield mobilites as high as 175 $cm^2/V\cdot s$ with *n*-type carrier concentrations of $5x10^{17}$ cm^{-3}.

III.2 Variation of the Indium Content

Following the optimization of the growth of the $Ga_{0.8}In_{0.2}N$, we proceeded to grow samples in which we varied the Ga/In ratio. In a series of experiments, we changed value of x form $x = 1.0$ to $x = 0.1$ in increments of 0.1. The films were grown under the optimum conditions as prescribed by the DOE. The purpose of this investigation is to determine the

effects of a variation in the constituent materials. Since this is the key to determining the operational wavelength of an optical device, knowledge and control of these characteristics are crucial. Table III-3 shows the PL bandgap peak and midgap peak intensities with the corresponding energies for samples with x as low as 0.4. Samples with x-values less than 0.4 showed no PL.

Table III-3: PL peaks for films with varying indium content

x	Pk(mV)	E_g(eV)	Pk_1(mV)	E_1(eV)	Pk_2(mV)	E_2(eV)
1.0	132.4	3.47	22.0	2.20	—	—
0.9	99.7	3.31	3.4	2.72	3.0	2.51
0.8	97.1	3.10	3.4	2.66	2.3	2.47
0.7	53.7	2.97	8.6	2.54	7.8	2.40
0.6	29.4	2.77	7.9	2.41	7.8	2.27
0.5	14.7	2.59	5.8	2.29	5.5	2.17
0.4	5.8	2.47	—	—	—	—

Figure III-2 shows the dependence of the PL bandgap peak intensity on the indium mole fraction for the films grown in this experiment. GaN (x=1) films had a strong sharp peak at 358 nm corresponding to the exciton near the band edge. Another frequently observed luminescent band occurs in the midgap region centered around 2.2 eV. As the indium mole fraction was increased, the bandgap peak became weaker and shifted toward longer wavelengths. As the indium mole fraction increased, these midgap bands also shifted toward longer wavelengths, but not at the same rate as the bandgap peaks.

Table III-4 shows the c_0 lattice parameters as measured by θ-2θ X-ray scans as well as Hall mobilities and carrier concentration for the same samples. Again, samples with x-values less than 0.4 showed no XRD peaks and Hall measurements were inconclusive, because those samples were highly resistive, both results are indicators of poor crystal quality.

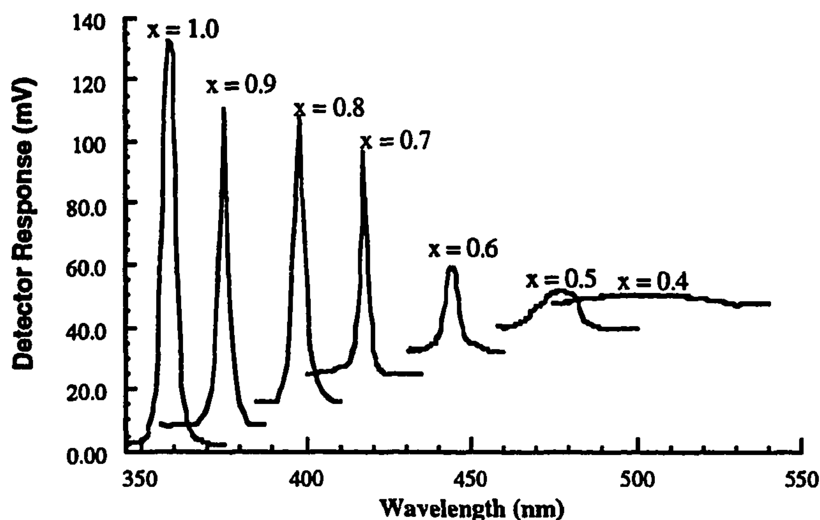

Figure III-2: PL intensity as a function of luminescent wavelength. Note that the baseline of each peak is offset by 8 mV in order to clarify the graph.

Table III-4: In-plane lattice parameters and Van der Pauw-Hall data

x	c_o (Å)	μ ($cm^2/V{\cdot}s$)	n (cm^{-3})
1.0	5.185	30	3.3×10^{17}
0.9	5.220	75	3.6×10^{17}
0.8	5.261	175	5.1×10^{17}
0.7	5.310	69	8.7×10^{17}
0.6	5.360	31	5.3×10^{18}
0.5	5.410	12	3.4×10^{19}
0.4	5.491	4	8.4×10^{19}

The shift in lattice constant is consistent with larger mole fractions of indium. However, the measured c_O values fell short of those predicted by our calculations. This could be due to re-evaporation of the In species at the substrate surface. Also, after many consecutive growths as was the case here, the indium source is depleted and the In molecular flux at the substrate is diminished suggesting that the indium growth rate needs to be recalibrated.

The Hall mobilities initially increased with indium content but began to fall off after $x = 0.7$. In general, one would expect the mobility to increase as indium mole fraction increases because the electron effective decreases as x decreases. (The electron effective mass ratio for pure InN is 0.1 while that for pure GaN is 0.22). However, we observed both a sharp decrease in Hall mobilities and an increase in electron concentration as the films became indium rich. Again, this is consistent with the decrease in crystal quality for the samples with high In content.

Figure III-3 shows the variation in bandgap verses the c-axis lattice parameter. As can be seen, the data does not follow a straight line, but rather show some bowing, which is typical in III-V alloy semiconductors. Performing a quadratic curve fit to our data, we obtain,

$$E_G(x) = 1.87eV + (1.35eV)x + (0.25ev)x^2. \qquad \text{(III-1)}$$

Equation (III-1) should be used with some caution. First, in looking at the variation of lattice constant with x, we do not obtain a straight line, which is what we would typically expect for an alloy. However, the variance of the measured lattice constant from the linear is less than one percent at any value of x. Secondly, the determination of the peak wavelength for smaller values of x is problematic because of the weak luminescence and broad peaks seen those PL measurements (see Fig. III-2).

III.3 Temperature Dependence of Luminescence

III.3.1 Variation of Luminescence Intensity with Temperature

Temperature-dependent measurements of PL were performed on one of our best $Ga_{0.8}In_{0.2}N$ films grown under the optimized DOE specified growth conditions. The purpose of this study was to investigate the various recombination processes as a function of temperature. A PL spectrum from this sample is shown in Figure III-4.

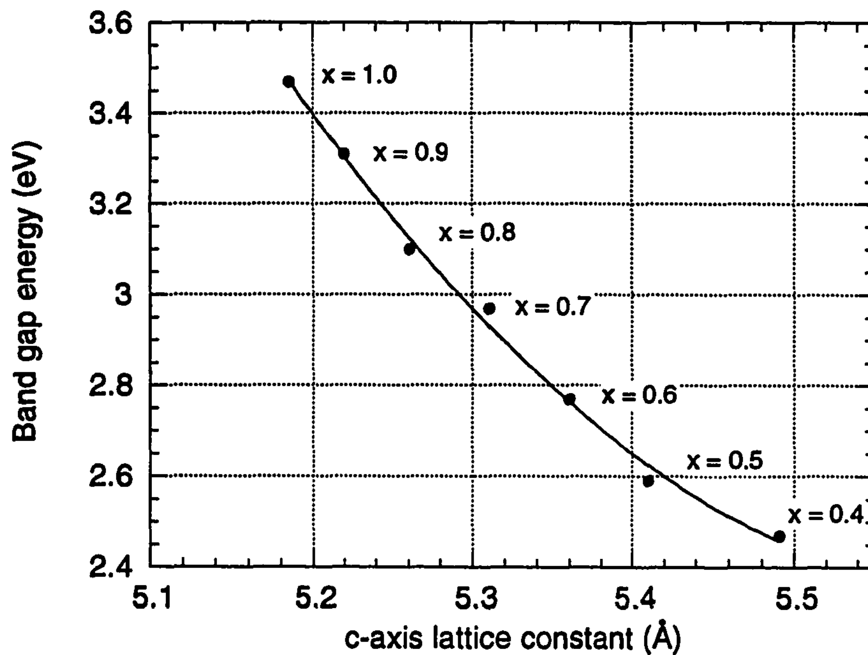

Figure III-3: Variation in bandgap and c-axis lattice parameter.

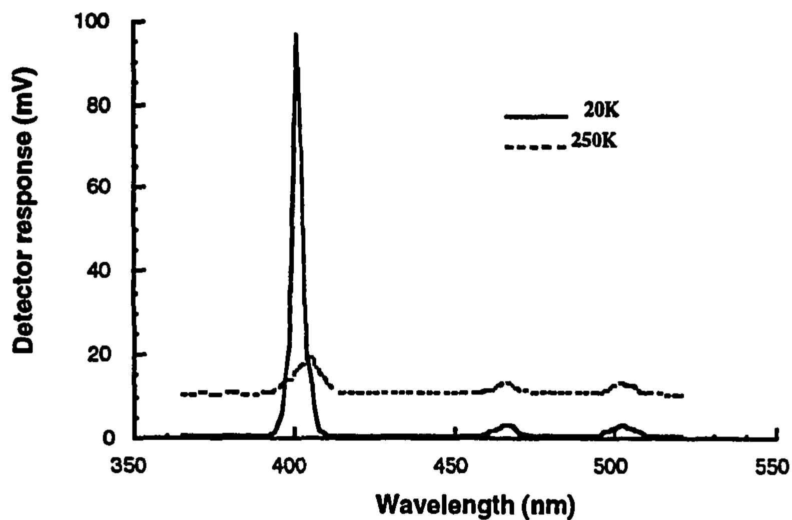

Figure III-4: Temperature dependence of the bandgap and the deep level PL for a $Ga_{0.8}In_{0.2}N$ grown under optimized conditions.

It can be seen in Fig. III-4 that the excitonic recombination next to the band edge is dominant at lower temperatures but diminishes at high temperatures. However, the midgap defect related peaks show very little thermal dependence.

Figure III-5a shows the PL sprecta from the exciton peak for various temperatures. The dependence of this peak on temperature is very significant and is useful in determining the activation (binding) energy E_A of the exciton as emission intensity decreases at higher temperatures. Since emission is proportional to carriers in the conduction band, it can be related to the temperature by the relation, $I = A^*\exp\{-E_A/kT\}$.

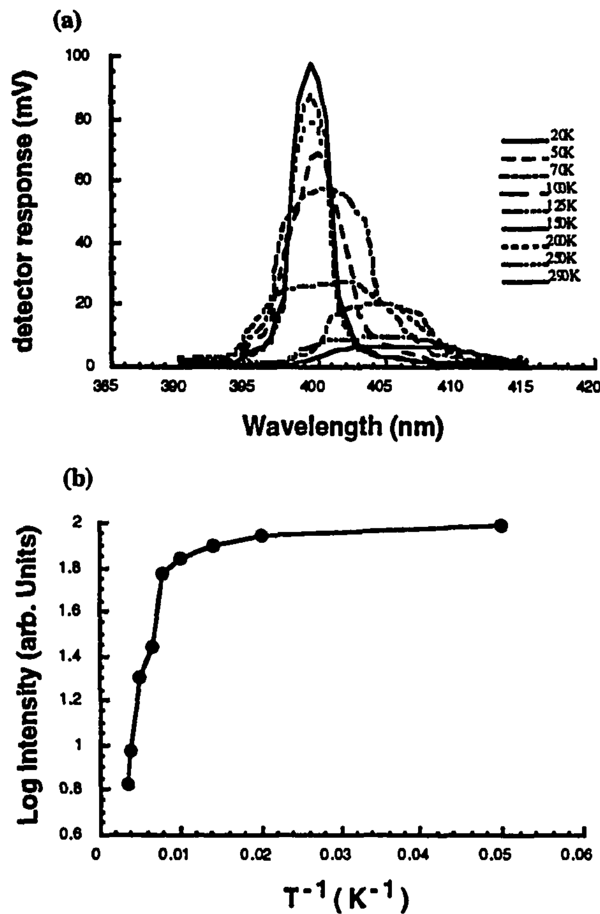

Figure III-5: Temperature dependence of the excitonic peak near the band edge: a) Peak dependence at various temperatures, b) log intensity vs. reciprocal temp.

Figure III-5b is a plot of the logarithm of emission intensity versus the reciprocal temperature. The activation energy is calculated from the gradient of the plot in the higher-temperature region of the curve, yielding a value of 18.7 meV. Similar calculations for activation energy for pure GaN yield about 24 meV.[43] This value is quite close to the binding energy of an exciton bound to a neutral donor, although it may have a different interpretation than the binding energy itself.

III.3.2 Variation of the Bandgap with Temperature of $Ga_{0.8}In_{0.2}N$

The temperature dependence of the bandgap is reported here and specifically applies to the variation of the excitonic peak over the range of temperatures 20K to 290K. There are no reported results of these nature for (Ga,In)N in the literature. Figure III-6 is plot of the excitonic PL energy versus the variation in temperature. This plot shows a roughly linear dependence of the peak wavelength for temperatures above 125K. (Note that the peak wavelength is the bandgap energy minus the exciton energy, which we are assuming is approximately constant in this range.) The value for the decrease in bandgap with increasing temperature is calculated from a curve fit for this plot. The calculated value is given as dE_g/dT = -3.51×10^{-4}eV•K^{-1}. This compares with the value of pure GaN which is given by dE_g/dT = -3.8×10^{-4}eV•K^{-1}.

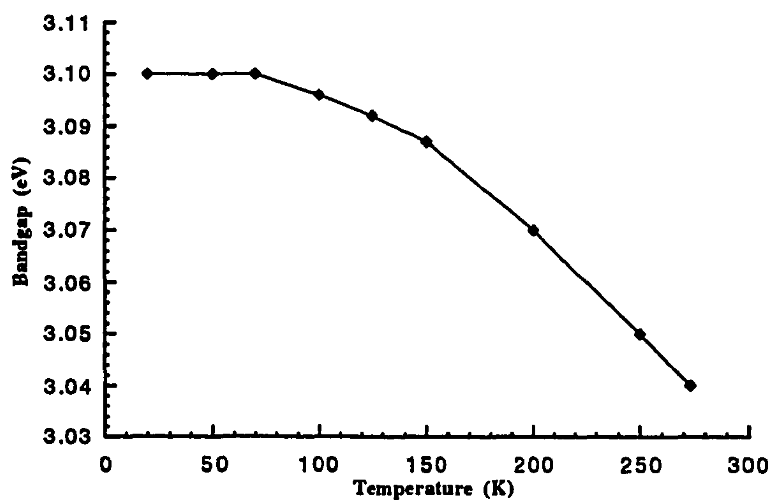

Figure III-6: Plot of the energy shift of the excitonic recombination with temperature

IV. SUMMARY

IV.1 DOE

These studies include a designed experiment which demonstrates the photoluminescence dependence of the films on the growth conditions as well as the control parameters of the ECR. Excitonic transitions are the most common features of the PL spectra from these films. The introduction of indium results in two broad luminescence bands below the excitonic peak. Although the origin of these deep level recombination states is uncertain, they do act as very effective luminescence centers and can be associated with material quality. The better quality material tends to exhibit negligible luminescence associated with deep level defects. On the other hand, in very defective material, the midgap bands dominate the PL spectrum.

On the basis of the relative intensities of the bandgap and midgap luminescence peaks, our designed experiment showed that the crystal quality of the films was strongly dependent on the combined influence of both the ECR microwave power and DC current to the magnetic coil, a result that has not been previously reported in any ECR nitride work. Moustakas *et al.* had made mention of the strong dependence of film quality on the ECR microwave power but made no mention of the magnetic field strength.[20] This magnitude field dependence suggests that the proximity of the ECR condition relative to the substrate surface can have a profound effect on growth kinetics. It is conceivable that at higher magnet currents, where the ECR condition is much closer to the substrate, more high-energy nitrogen atoms impinge on the epilayer and impart structural damage to the film. As the magnet current is reduced, the ECR condition is moved farther away from the substrate, and this seems to greatly improve the film quality. This reason for this improvement is not yet clear, but we speculate that the energy of the nitrogen atoms impinging on the sample surface is lower when the ECR is farther away. The result, as shown in the DOE procedure, in improved band-to-band luminescence.

Our results show that the buffer layer thickness had much less effect on the overall

quality of the (Ga,In)N layers. The results of the DOE indicate that the contribution of the buffer layer does not change after about 600Å. This has also been reported in III-V antimonide-based quantum wells grown on foreign substrates.[45] It would be worthwhile to investigate the effects of growing a superlattice on top of the buffer layer as this has improved film quality in the same antimonide based QWs.

Substrate temperature had a more profound effect on the relative In to Ga content as the temperature range in this experiment was too narrow to observe a significant change in film quality. Because indium tends to re-evaporate at higher temperatures (> 600°C), we were not able to investigate the temperature regime which has produced high quality GaN films. As it was, even at relatively low substrate temperatures, our samples showed a significant reduction in In content compared to what was expected.

IV.2 Variation in Indium Content

Our initial GaN films had sharp, strong PL peaks at 358 nm corresponding to an exciton transition at $E_g = 3.47$ eV. Another frequently observed luminescence band in those GaN layers, as has also been reported by a number of researchers, was a broad yellow emission. This broad band disappears with the introduction of indium into the films and is replaced by two slightly narrower bands at higher energy, one at 2.27 eV and one at 2.51 eV for x=0.8. As the indium content is increased, the excitonic peak shifts to larger wavelengths and decreases in intensity. The characteristic midgap peaks also shift to longer wavelengths but the PL intensities do not change as much as the bandgap intensities do with varying In content. This suggests that there is a general reduction in radiative recombination from the band edge and that the radiative defect recombination begins to dominate. With even higher indium mole fractions ($x<0.4$) the midgap peaks also disappear, suggesting the non-radiative events dominate the recombination process. This is possibly due to major structural defects such as dislocations, stacking faults, and even polycrystallinity.

X-ray θ-2θ and the Van der Pauw-Hall data also support the notion that increasing In

content leads to poor quality films. The θ-2θ diffraction peaks shift to smaller angles as the lattice constant of the films becomes larger. At the same time these peaks become broader and less intense, indicating that X-ray scattering becomes more random which is characteristic of less crystalline order. Hall measurements indicated that the films shifted from a highly conductive to highly resistive as the InN content in the films became greater than 60%, again indicating poor crystalline quality. It may be possible that another DOE experiment specifically designed for this regime might determine growth parameters which could improve the quality of indium rich films.

IV.3 Recommendations for Future Work

Bulk layers $Ga_xIn_{1-x}N$ grown by electron cyclotron resonance plasma assisted molecular beam epitaxy has been conducted in this experiment. The focus of this research has been on values of x which correspond to the blue and blue-green spectral region. Data for values of x ranging from 1.0 to 0.4 are presented. Data for smaller x-values were unattainable as the material quality of the films became poor with increasing indium content. These studies will be useful for providing information on material quality and defects in materials for optoelectronic device operation in this spectral region.

In principle, the DOE procedure should be extended to cover other compositions of (Ga,In)N. In particular, the compositional range for $x < 0.4$ (In-rich) needs further attention. The next step would be to extend this work to quantum well and superlattice structures. Again, the DOE method should prove invaluable to optimizing multi-layer growths with all of the attendant process variables.

Another important aspect which has not been addressed is p-type doing in the (Ga,In)N layers. Currently Mg is the p-type of choice for nitride materials. However, Mg has a strong memory effect in MBE systems (residual doping levels in films grown after the Mg has been used). It would be worthwhile to look at other candidate dopants, in particular Be. Be is the standard p-type dopant for most III-V compounds, and mysteriously, has received little or no attention for use in the nitrides.

Of course, there is the eventual step to making devices. But this author believes that concentrating on fundamental issues is extreme importance.

On the equipment front, improvements to some components of our PL system would be beneficial. Most useful would be the replacement of the low-power, pulsed nitrogen laser with a higher-power CW unit, either a He-Cd or argon laser with UV optics. This would greatly improve the sensitivity of our PL measurements. Also very crucial is making available X-ray diffraction tools at the MRC. In particular, a double-crystal rocking curve instrument would be invaluable. Then structural parameters determined from X-ray measurements could by added to the DOE procedure. This should add some clarity to the to current picture.

REFERENCES

(1) Strite, S.; Morkoc, H. *J. Vac. Sci. Technol. B,* **1992,** *10,* 1237-1265.

(2) Powell, R. C.; Lee, N. E.; Kim, Y. W.; Greene, J. E. *J. Appl. Phys.* **1993,** *73,* 189-204.

(3) Kim, J. G.; Frenkel, A. C.; Liu, H.; Park, R. M. *Appl. Phys. Lett.* **1994,** *65,* 91-93.

(4) Kubota, K.; Kobayashi, Y.; Fujimoto, K. *J. Appl. Phys.* **1989,** *66,* 2984-2988.

(5) Nakamura, S.; Mukai, T.; Senoh, M. **1992,** *Jap.J. Appl. Phys.31,* 2883-2888.

(6) Abernathy, C. R.; MacKenzie, J. D.; Bharaten, S. R.; Jones, K. S.; Pearton, S. J. *Appl. Phys. Lett.* **1995,** *66,* 1632-1634.

(7) Guo, Q.; Ogawa, H. *Appl. Phys. Lett.* **1995,** *66,* 715-717.

(8) Kistenmacher, T. J.; Bryden, W. A. *Appl. Phys. Lett.* **1993,** *62,* 1221-1223.

(9) *Properties of III-V Nitrides;* Inspec Publications: New York, 1995.

(10) Lei, T.; K. F. Ludwig, J.; Moustakas, T. D. *J. Appl. Phys.* **1993,** *74,* 4430-4436.

(11) Paisley, M. J.; Sitar, Z.; Posthill, J. B.; Davis, R. F. *J. Vac. Sci. Technol. A* **1989,** *7,* 701-705.

(12) He, Z. Q.; Ding, X. M.; Hou, X. Y.; Wang, X. *Appl. Phys. Lett.* **1994,** *64,* 315-317.

(13) Powell, R. C.; Tomasch, G. A.; Kim, Y. W.; Thornton, J. A.; Greene, J. E. *MRS Symp. Proc.* **1990,***162,* 525.

(14) Lei, T.; Moustakas, T. D.; Graham, R. J.; He, Y.; Berkowitz, S. J. *J. Appl. Phys.* **1992,** *71,* 4933-4943.

(15) Kuznia, J. N.; Khan, M. A.; Olson, T. D.; Kaplan, R.; Freitas, J. *J. Appl. Phys.* **1993,** *73,* 4700-4702.

(16) Molner, R. J.; Lei, T.; Moustakas, T. D. *MRS Symposium on Semiconductor Heterostructures for Photonic and Electronic Applications*; **1993,** *281.*

(17) Maruska, H. P.; Teitjen, J. J. *Appl. Phys. Lett.* **1969**, *15*, 327.

(18) Wickenden, D. K.; Bargeron, C. B.; Byrden, W. A.; Miragliotta, J. *Appl. Phys. Lett.* **1994**, *65*, 2024-2026.

(19) Wang, C.; Davis, R. F. *Appl. Phys. Lett.* **1993**, *63*, 990-992.

(20) Moustakas, T. D.; Lei, T.; Molnar, R. J. *Physica B;* **1993**, *185*, 36-49.

(21) Nakamura, S.; Mukai, T.; Senoh, M. *J. Appl. Phys.* **1994**, *76*, 8189-8191.

(22) Pankove, J. I.; Miller, E. A.; Richman, D.; Berkeyheiser, J. E.; Lumin, J. *J. Appl.-Phys.* **1971**, *4*, 36-39.

(23) Nakamura, S.; Mukai, T.; Senoh, M. *J. Appl. Phys.* **1994**, *64*, 1687-1689.

(24) Molnar, R. J.; Singh, R.; Moustakas, T. D. *Journal of Electronic Materials;*,**1995**, 24, 628-633.

(25) Haase, M. A.; Baude, P. F.; Hagedorn, M. S.; Qiu, J.; DePuydt, J. M.; Cheng, H.; Guha, S.; Hofler, G. E.; Wu, B. J. *Appl. Phys. Lett.* **1993**, *63*, 2315-2317.

(26) Guha, S.; DePuydt, J. M.; Haase, M. A.; Qiu, J.; Cheng, H. *Appl. Phys. Lett.* **1993**, *63*, 3107-3109.

(27) Hunt, R. W.; Vanzetti, L.; Castro, T.; Chen, K. M.; Sorba, L.; Cohen, P. I.; Gladfelter, W.; Hove, J. M. V.; Kuznia, J. N.; Khan, M. A.; Franciosi, A. *Physica B: Condensed Matter,* **1993**, *185*, 415-421.

(28) Guo, Q.; Yoshida, A. *Japanese Journal of Applied Physics* **1994**, *33*, 2453-2456.

(29) Khan, M. A.; Krishnankutty, S.; Skogman, R. A.; Kuznia, J. N.; Olson, D. T.; George, T. *Appl. Phys. Lett.* **1994**, *65*, 520-521.

(30) Akasaki, I.; Amano, H. *Appl. Phys. Lett.* **1992**, *64*, 327-329.

(31) Amano, H.; Tanaka, T.; Kunii, Y.; Kato, K.; Kim, S. T.; Akasaki, I. *Appl. Phys. Lett* **1994**, *64*, 1377-1379.

(32) Reitz, L. F. *Society of Photo-Optical Instrumentation Engineers* **1993**, *1952*, 14-22.

(33) Khan, M. A.; Bhattari, A.; Kuznia, J. N.; Olson, D. T. *Appl. Phys. Lett.* **1993**, *63*, 1214-1215.

(34) Khan, M. A.; Kuznia, J. N.; Olson, T. D.; George, T.; Pike, W. T. *Appl. Phys. Lett.* **1993**, *63*, 3470-3472.

(35) Lei, T.; Fancuilli, M.; Molnar, R. J.; Moustakas, T. D.; Graham, R. J.; Scanlon, J. *Appl. Phys. Lett.* **1991**, *59*, 944-946.

(36) Molnar, R. J.; Singh, R.; Moustakas, T. D. *Journal of Electronic Materials* **1995**, *24*, 275-281.

(37) Molnar, R. J.; Moustakas, T. D. *J. Appl. Phys.* **1994**, *76*, 1-9.

(38) Loretto, M. H. *Electron Beam Analysis of Materials:* Chapman and Hall; London, **1984**.

(39) Schroder, D. K. *Semiconductor Material and Device Characterization;* John Wiley and Sons: New York, **1990**.

(40) Weeks, J. D. *Order in Strongly Fluctuating Condensed Matter Systems;* Plenum; New York, **1980**.

(41) Eddy, C. R. : Moustakas, T. D. *J. Appl. Phys.* **1993**, *73*, 448-454.

(42) Dingle, R. ; Sell, D. D. ;Stokowski, S. E. ;Ilegems, M. *Phys. Rev.* B **1971** 4, 1211

(43) Singh, R.; Molnar, R. J. ;Unlu, M. S.; Moustakas, T. D. *Appl. Phys. Lett.* **1994**, *64*, 336-338

(44) Lin, M. E.; Sverdlov B.; Zhou G. L.; Morkoc H. *Appl. Phys. Lett.* **1993**, *62*, 3479-3481.

(45) Liners, W. O. Master of Science Thesis, Iowa State University, **1993**.

ACKNOWLEDGEMENTS

I would like to take this opportunity to thank my major professor, Dr. Gary Tuttle, for his guidance and assistance throughout this project and my graduate school career. I would also like to thank Dr. Dalal, Dr. Chumbley, Dr. Hsieh, and Dr. Kai-Ming Ho for their time and patience in serving as my graduate committee members.

I want to acknowledge several people who performed rocking curve measurements on GaN samples for me: Bobby Brar at UC Santa Barbara, Erick Michel at Northwestern, and Jim Gaines at Phillips Laboratories. I want to thank Scott Chumbley (again) and Fran Laabs of Ames Laboratory for all their help with other X-ray measurements. I am greatly indebted to Prof. John Patterson, who explained the principles of DOE and helped me use ECHIP to set up the experiments used to optimize the growth of (Ga,In)N.

A special thanks goes to my parents, Hank and Vivian Liners, and my parents in-law Robert and Patrica Anderson for their love and support throughout my entire college career. Finally, I would like to thank my friends and colleagues, Russ Bruhn, Scott DeBoer, Jon Kavanaugh, Sandhya Gupta, Sanjeev, Ping, Shi-di, Zafar, and Doug Robinson and all the others who have all made my working environment more enjoyable.

My most special thanks goes out to my beloved wife Kathe and my son Tom. Kathe's love and understanding during late nights, endless frustrations, and hard times have inspired me to achieve goals otherwise unattainable. She has allowed her own dreams and aspirations to be delayed and even dwarfed in the eyes of friends and family that my education would continue unhindered. Also, Tom's wit and humor have kept my own child alive and active in banter and play.

APPENDIX A
PHOTOLUMINESCENCE

A.1 Photoluminescence

A.1.1 Description

Photoluminescence (PL) is a nondestructive technique for the determination of impurities present in semiconductor materials. In general, a light beam incident on a piece of material induces excitation of electrons to higher energy levels of the system, where upon a light spectrum characteristic for the so populated energy level system of the material is emitted in the subsequent de-excitation process[1] (Fig A-1).

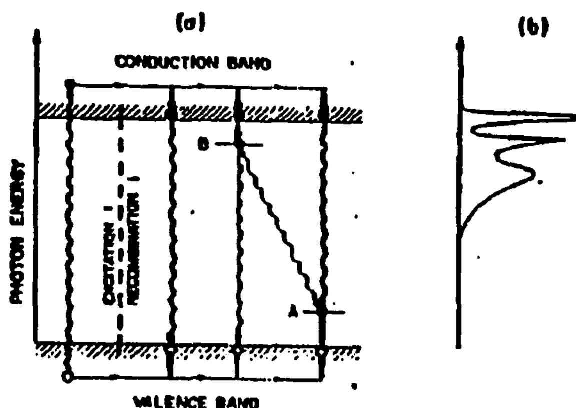

Figure A-1: Schematic representation of photoluminescence process depicting a) optical excitation induced by a photon and the various transitions and b) the PL spectra induced by the different recombination processes in part (a) (Reproduced from Reference 1)

As a phenomenon, photoluminescence in solid materials has been known for many decades, with a strong emphasis in the early work on studies of internal radiative transitions for

ions in insulators.[2] A major step forward in the utilization of this technique for characterization of semiconducting materials was taken with the availability of CW gas lasers in the 1960's. Laser excitation was not only convenient, but also allowed sufficient intensities for studies of details of radiative transitions at high spectral resolution. This became necessary in order to obtain a physical interpretation of the mechanisms for luminescence spectra in semiconductors. Within the last twenty-five years experimental data from these investigations for virtually every known semiconductor has been catalogued and published. Photoluminescence has been established as one of the most powerful and versatile techniques to investigate intrinsic as well as defect-related properties of semiconductor materials.

A.2 Theory

A.2.1 Radiative Recombination

PL is particularly useful for the detection of shallow-level impurities, but can also detect certain deep-level impurities, provided that radiative recombination events dominate non-radiative recombination. Fortunately many impurities exhibit radiative recombination and are therefore detectable by this technique. Qualitative information can be extracted by this method in that it identifies impurities however, it does not provide quantitative information on the impurity concentration. PL provides simultaneous information on many types of impurities contained in a single sample in one quick measurement.[3]

The sample is placed in a cryostat and cooled to temperatures near liquid helium. Low-temperature measurements are essential in order to obtain the fullest spectroscopic information by minimizing thermally-activated non-radiative recombination processes and thermal line broadening. The thermal distribution of carriers excited into a band contributes a width of approximately $kT/2$ to an emission line originating from that band. This makes it necessary to cool the sample to reduce the line width. For example, the thermal energy $kT/2$ is only 1.8 meV at $T = 4.2$ K. For most measurements this is sufficiently low, but occasionally it is

necessary to reduce this broadening further by reducing the sample temperature below 4.2 K.[3]

III.2.2 Transitions

As stated previously, the sample is excited with an optical source, typically a laser with $h\nu > E_g$, generating electron-hole pairs (EHPs) that recombine by one of several mechanisms. Photons are emitted only when a radiative recombination event occurs. In general, low-temperature recombination is radiative. Five of the most commonly observed PL transitions[4] are illustrated in Figure A-2.

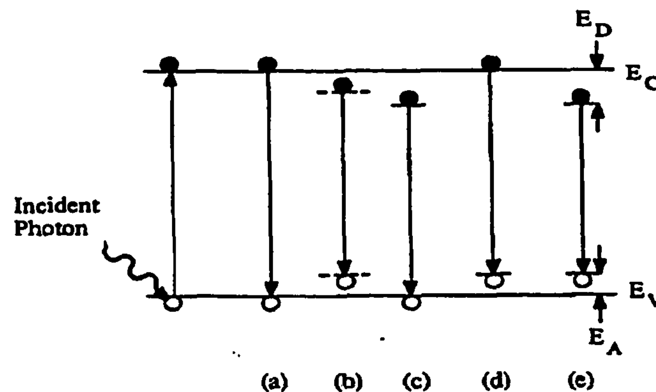

Figure A-2: Radiative transitions observed with photoluminescence (Reproduced from Reference 20)

Photon energy depends upon which of these transitions occurs and all can be observed simultaneously. Band-to-band recombination (Figure A-2a) dominates at room temperature but is rarely observed at low temperatures in materials with small effective masses due to the large electron orbital radii. Excitonic recombination is commonly observed (Figure A-2b), this is when an EHP is bound together by Coulombic attraction in a hydrogen-like state.[5] Its energy is slightly less than the band-gap energy required to create an EHP. An exciton can move through the crystal, but being a *bound* EHP, both electron and hole move together and no photoconductivity results. A free hole can combine with a neutral donor (Figure A-2c) to form

a positively charged excitonic ion or bound exciton (BE).[6] The electron bound to the donor travels in a wide orbit around the donor. Similarly electrons combining with neutral acceptors also form bound excitons.

If the material is sufficiently pure, free excitons form and recombine by emitting photons. The photon energy in direct band-gap semiconductors is[6]

$$h\nu = E_g - E_{x} \qquad \text{(A-1)}$$

where E_{x} is the excitonic energy. In indirect band-gap semiconductors, momentum conservation requires the emission of a phonon, giving[6]

$$h\nu = E_g - E_{g} - E_p \qquad \text{(A-2)}$$

Where E_p is the phonon energy. Bound exciton recombination dominates over free exciton recombination for less pure materials. A free electron can recombine with a hole on a neutral acceptor (Figure A-2d), and similarly a free hole can recombine with an electron on a neutral donor (Figure A-2c).

Lastly, an electron on a neutral donor can recombine with a hole on a neutral acceptor, the well-known donor-acceptor (D-A) recombination, illustrated in Figure A-2e. The energy line has an energy modified by the Coulombic interaction between donors and acceptors[7]

$$h\nu = E_G(E_A + E_D) + \frac{q^2}{K_s \varepsilon_o r} \qquad \text{(A-3)}$$

where r is the distance between donor and acceptor. The photon energy in Equation A-3 can be larger than the band gap for small $(E_A + E_D)$. The full width at half maximum (FWHM) for bound exciton transitions are typically $\leq kT/2$ and resemble slightly broadened delta functions. This distinguishes them from donor-valence band transitions which are usually a few kT wide. Energies for these two transitions are frequently similar, and the line widths are used to determine the transition type.[3]

A.3 Experimental Methods and Techniques

A.3.1 System Description

A simple setup for a photoluminescence measurement system, identical to that in our laboratory, is depicted in Figure A.3. Photo excitation of the sample is accomplished by an optical source, in this case a laser, although a lamp together with a monochrometer is sufficient. The excitation photon energy is chosen to be greater than the band gap of the sample under investigation.

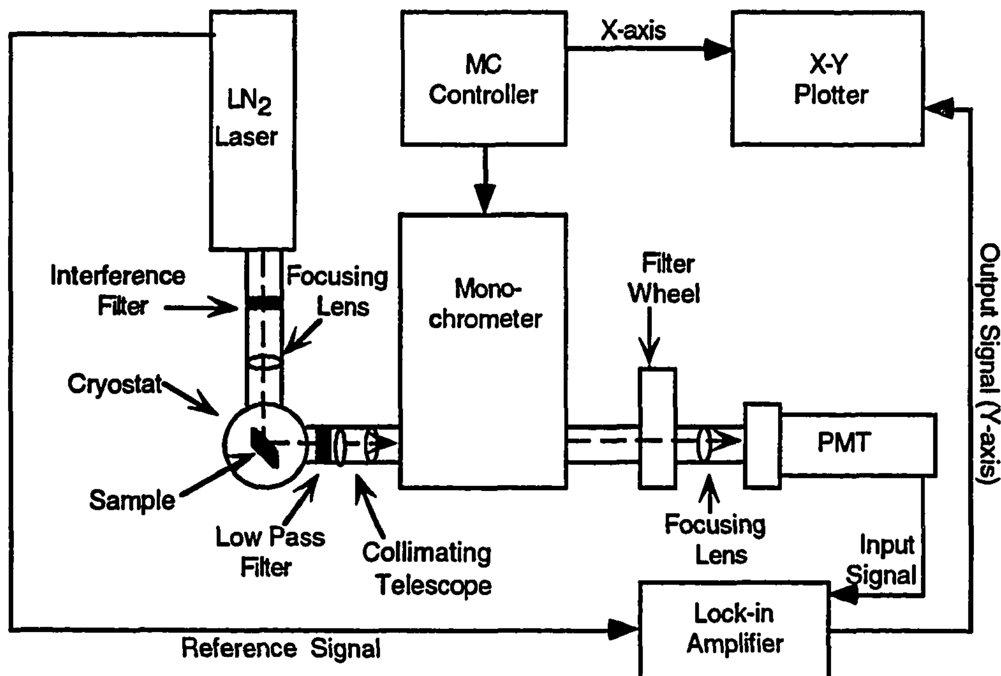

Figure A-3: Schematic representation of a photoluminescence apparatus built in our laboratory

The sample is placed in a cryostat for low temperature measurements, which are necessary to prevent thermal ionization of the optically active centers and, as mentioned previously, to minimize the broadening of the sharp spectral features by phonons. The system consists of a monochromator and a detector, generally a photomultiplier tube (PMT) or a photo diode,

depending on the wavelength region of interest and the required sensitivity.

The exciting light may further be chopped or pulsed for phase-sensitive detection (as in our system) or lifetime measurements. In some systems a beam splitter is placed in the path of the incident light in order to provide a reference signal to be synchronized with the pulsed or chopped light from a lamp or CW laser. Our laser is equipped with an electronic output signal which corresponds to the light pulse. Also, should we ever acquire a decent CW HeCd laser, we also have a sophisticated chopper system with a synchronous electronic output. Ideally, a computer is used to control the apparatus, which includes controlling the monochrometer and reading the output from the signal detection system. Our system employs a controller which specifically operates the monochrometer and the output at this point is simply a voltage signal. It is anticipated that at least an X-Y chart recorder will be available.

A.4 The Detection System

As already mentioned, the experiment described herein utilizes a phase sensitive detection or lock-in technique. The following sections provide a detailed account of the different parts of the experimental setup depicted in Figure 3.

A.4.1 Sample and its Temperature Control

The sample consists of approximately one square centimeter of the thin film which is cut from the parent sample although the entire sample can be used. Preparation usually involves degreasing the sample in a sequence of boiling TCA, acetone and methanol followed by a DI water rinse and spin dried. The sample is then glued with silver paint to a copper mount designed to attach to the cold finger of the cryostat. The silver paint acts as a good conductor of heat and prevents localized heating by the laser.

The sample is cooled in a CTI compressor driven closed cycle cryostat. The temperature is controlled using a T. R. I. model 2000 Temperature Controller. Ideally, this

system has a temperature range of 8-300 K. The cryostat has two quartz windows oriented 90° to each other, thus the excitation beam can easily be aligned such that it does not interfere with the detection optics.

A.4.2 Excitation Laser and Related Optics

A PRA model LN 103 pulsed nitrogen laser is used as the excitation source. The specifications of the nitrogen laser are a crucial factor in the choice of a proper detection system. The dominant line in the laser is 337.1 nm corresponding to 3.68 eV. The laser pulse width ranges between 100 ns and 10 μs and a rated peak power of 250 kW at a pulse repetition frequency of 50 Hz. The pulse energy at these specifications is about 85 μJ. The nitrogen laser requires a flow of nitrogen gas through the lasing region and the spark gap area must be pressurized to 30 PSI. The flow rate through the laser is very critical to stable operation otherwise it can misfire or lose pulse energy altogether. An empirical value of the flow rate must be determined which will ensure good stability over long periods of time.

The excitation wavelength of the nitrogen laser lies in the ultraviolet (UV) region of the electromagnet spectrum. This requires severe restrictions on the optics used in this experiment. All optical components made of glass become quite useless because of their greatly enhanced absorption below 350-360 nm. Thus it is required to use all fused silica or quartz mirrors and lenses.

The laser beam can be made circular using one of the adjustable iris-type apertures in our laboratory. The aperture is set at approximately 6.0 mm resulting in a circular collimated beam. The beam passes through an interference filter in order to filter out any lines other than 337.1 nm present in the laser. Finally. the beam is focused on the sample with a 12 cm focal length lens. The spot size is about 0.5 mm in diameter.

A.4.3 Collection Optics

A lens collection system consisting of two plano-convex fused silica lenses acting as a telescope collects the photoluminescence from the sample as is shown in Figure A-3. A glass long wavelength filter is placed between the lens and the sample. This filter has a very sharp cutoff below 345 nm (as was confirmed from the filter response provided by the manufacturer). This filter is very effective in preventing any scattered laser light from entering the monochrometer. The objective from the telescope slides on a barrel arrangement which can be adjusted to optimize PL collection from the sample. Also, the whole monochrometer housing can be pivoted to change the angle at which the light is collected which in turn maximizes the light collected at the detector. The calibration procedure for this process can be achieved by setting the monochrometer to correspond to the excitonic recombination process wavelength (358 nm) for GaN and adjust the apparatus for a maximum reading on the lock-in amplifier.

A.4.4 Spectrometer Control

The spectrometer (Jerrel-Ash model MC 20) uses a grating having 1200 grooves /mm, which disperses 1 nm band for 0.3 mm of slit width and 3.3 nm for 1 mm of slit width. Most experiments are conducted with the entrance slit set at 0.15 mm. Since, according to the spectrometer manufacturer, the resolution is diffraction limited for slit width less than 0.3 mm, and thus the resolution of our particular setup is 10Å or 9.6 meV at the excitonic wavelength.

The stepper motor drive (Spectradata 22) is designed to control the spectrometer over the wavelengths of interest (from 340 nm to about 800 nm). The system consists of a geared motor drive and a stepper motor mounted on the spectrometer and is controlled by the Spectradata 22 control unit. The minimum step size of the motor is 1.8° which corresponds to a minimum wavelength increment of 0.025 nm. This step size is much smaller than the resolution of the spectrometer, which is about 10Å, as mentioned earlier. It should also be

pointed out that only the grating orientation is under control of the motor drive system. The slits are preset modules and are chosen according to the sample under investigation. For instance, the slit must be much larger for samples with weak luminescence than for ones with strong luminescence.

A.4.5 Photodetection and Instrumentation

A photomultiplier tube (Hamamatsu 1P28) is utilized as the light to current transducer. The PMT has a rated anode voltage of 1500 VDC however, most experiments in this setup are conducted between 750 and 1100 VDC. This voltage range is found to provide the maximum gain with minimum dark current. Also the life of the PMT is enhanced by a lowered bias voltage. The data can be normalized with the system response by taking into account the spectral response of the PMT. The spectral response of the Hamamatsu R 376 as specified by the manufacturer ranges from 185-800 nm which is well suited for our purposes.

The output of the PMT is converted to a voltage signal using a high speed JFET operational amplifier based integrator circuit as shown in Figure A-4. This is done to stretch the output current pulse from the PMT so that it can be accommodated in the limited bandwidth of the lock-in amplifier as described below.[8] The lock-in amplifier is provided with a with a reference signal from the signal output of the nitrogen laser which is a 40 V square pulse.

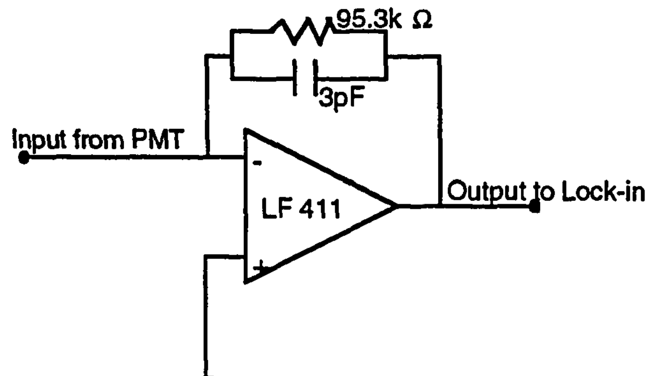

Figure A-4: Current to voltage converter and integrator circuit

A.4.6 Lock-in or Phase Sensitive Measurements[9]

The detection system used in our laboratory is referred to as a *phase-sensitive* or*locked-in* measurement technique (Princeton Applied Research 5207). In addition to this system, there are two other commonly used methods in optical measurements, *Box Car Integration* and *Photon Counting* which are discussed in great detail in Reference 30.

The amplifier can be preceded by a narrow band pass filter which can be tuned to the frequency of interest. One of the inputs to the lock-in amplifier is a trigger from the pulsed source or from a chopper which functions as the reference signal. The other input is the output from the photo detector and this of course is the measured signal. This technique is very immune to noise because the incident light is modulated before it illuminates the sample. At the detector end, only the light that is modulated is detected; similar to a radio receiver. Hence, most of the white Gaussian noise is eliminated by this technique.[8] However, a problem is inherent in a pulsed source with a very small duty cycle. In our case, a Nitrogen laser is employed with a pulse width of 10 ns while the pulse repetition frequency (PRF) is only 10 -100 Hz. In such a case, special signal shaping techniques of the JFET integrator can be utilized in order to accommodate the short pulses into the bandwidth of the lock-in amplifier which is on the order of about 120 kHz.

Finally, the analog output of the lock-in amplifier is connected to the Y-axis of an X-Y plotter and the spectrometer position form the Spectradata 22 control unit is connected to the X-axis. The entire system can be set at any desired sample temperature and can automatically run through the spectral range of interest.

Photoluminescence is an accurate and quick non-destructive characterization method for thin film studies. Observation of the various PL peaks from samples grown in our laboratory provide an excellent source of feedback for the growth of high quality crystal films. This characterization technique is a valuable tool in the optimization of ECR-MBE growth techniques. The contribution of this study will aid in the further development of short

wavelength optoelectronic devices based on III-V nitrides.

A.5 References

(1) Monemar, B. *Photoluminescence Techniques for studies of Composition and Defects in Semiconductors*; Academic Press: New York, 1980; Vol. 19A, 61-75.

(2) Klick, C. C.; Schulman, J. *Solid State Physics* **1957**, *5*, 97-173.

(3) Schroder, D. K. *Semiconductor Material and Device Characterization*; John Wiley and Sons: New York, 1990.

(4) Smith, K. K. *Thin Solid Films* **1981**, *84*, 171-182.

(5) Wolfe, J. P.; Mysyrowicz, A. *Sci. Am.* **1984**, *250*, 98-107.

(6) Pankove, J. I. *Optical Processes in Semiconductors*; Dover: New York, 1975.

(7) Dean, P. J. *Prog. Crystal Growth Charact.* **1982**, *5*, 89-174.

(8) Research, E. P. A. *Models 5207 & 5208 Lock-in AMplifiers Manual*; Doncastle House: Princeton N.J., 1985.

(9) Singh, R. Master of Science Thesis, Boston University, 1994.

APPENDIX B
ECR-MBE SYSTEM DESIGN AND ANALYSIS

B.1 Electron Cyclotron Resonance

B.1.1 System Design

The III-V nitride films in this experiment were grown by electron cyclotron resonance microwave-plasma-assisted molecular beam epitaxy. The ECR system employed in our growth method, built by Applied Science and Technology Inc. (ASTeX) is schematically illustrated in Figure B-1. The ASTeX Compact ECR™ plasma source is a high density, low

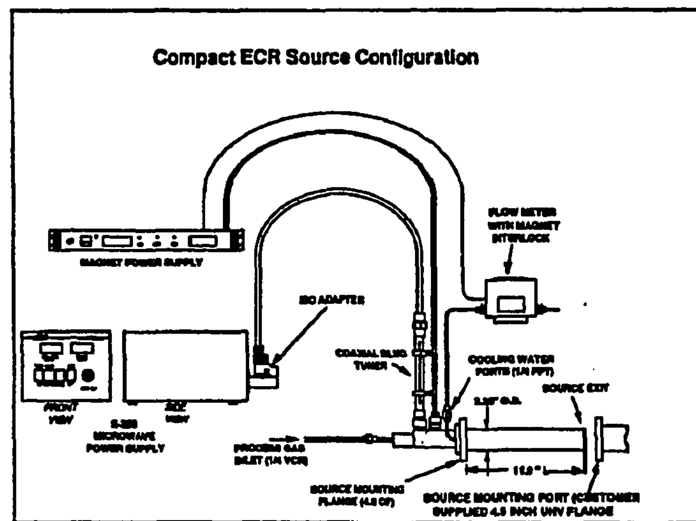

Figure B-1: Schematic representation of a compact ECR

pressure source designed for plasma enhanced chemical vapor deposition, plasma etching, surface cleaning, and molecular beam epitaxy.

Atomic and ionic nitrogen are produced by passing high purity molecular nitrogen gas through an axial electromagnet at the ECR source.[1] A high electron collision rate is achieved through efficient coupling of propagating plasma waves (2.45 GHz) and magnetic mirror

confinement. Typically, 10% of the molecular nitrogen gas is converted into atomic nitrogen.[2] Due to this high decomposition rate, a source pressure of about 10^{-3} Torr is sufficient to generate a stable plasma suitable for stoichiometric growth. A BN aperture, (1cm in diameter) placed at the ECR source exit, creates a pressure differential further reducing the growth pressure to about 10^{-4} Torr. The on axis ECR condition (H = 835 G) is about 20 cm from the substrate surface. The fundamental details of ECR electromagnetic theory are discussed at the end of this section for the benefit of the reader.

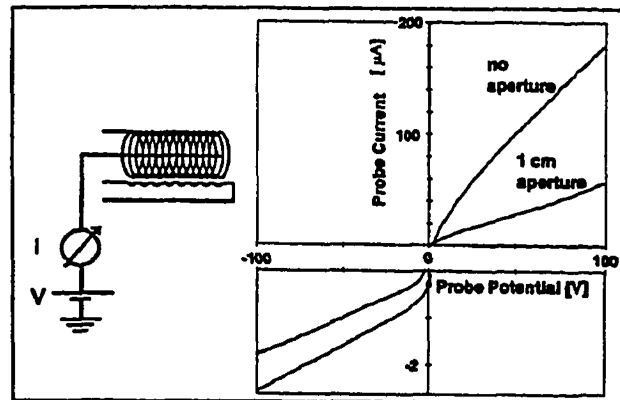

Figure II-2: Langmuir probe circuit with typical I-V characteristics

B.2 ECR Plasma Characterization

B.2.1 Langmuir Probe Studies

Langmuir probe studies were carried out by Molnar et al.[3] in an ECR-MBE system similar to ours and are summarized below. A nude ionization gauge placed in the position of the substrate is used as an electrostatic probe by connecting a DC power supply in series with an ammeter to the collector of the gauge. Figure B-2 shows a schematic of the measuring circuit and the I-V characteristics obtained with the ECR operating at 30 watts microwave power, both with and without the exit aperture.

Relative ion densities were determined by assuming the plasma is collisionless, the

electron energy distribution is Maxwellian, the plasma is quasi-neutral (N_i=N_e), the electron temperature is much greater than the ion temperature and the ions are singly charged. Then I^2 and V are related by the expression[4]

$$\frac{\partial I_i^2}{\partial V_p} = -\frac{3A^2 e^3 N_i^2}{4\pi m_i} \tag{B-1}$$

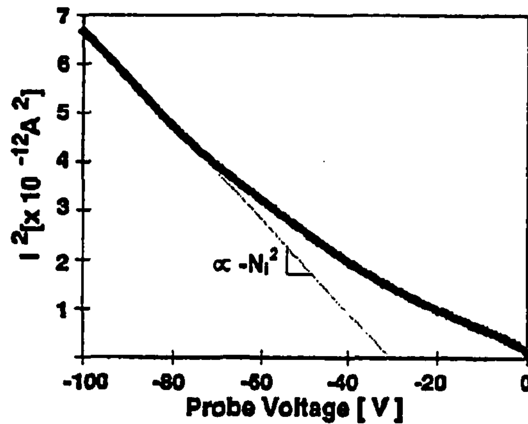

Figure B-3: I^2 vs. V in ion saturation (highly negative) region

Where I_i is the probe current in the saturated ion density (highly negative) regime, V_p is the applied probe potential, A is the area of the probe, N_i is the ion density, and m_i is the ion mass. The square of the relative ion density N_i^2 was determined from the slope of the line as shown in Figure B-3. The determination of the actual concentration of N_i requires the area of the probe to be known and due to uncertainty of the effect of components surrounding the probe, this expression was only used to compute relative ion densities. By employing such an interpretation on the data in Figure B.2, the ion density was calculated to be reduced by about 30% with the introduction of the exit aperture.[3]

B.2.2 Optical Emission Spectra

An optical emission spectra typical for an ECR generated nitrogen plasma is shown in Figure B-4. A UV fiber optic bundle was employed to collect light from a view port in the MBE system. The light was dispersed through a 0.25 m monochrometer and imaged onto a diode detector array. These emissions clearly indicate the presence of both ionic and neutral metastable molecular nitrogen species as well as the presence of atomic nitrogen.[5]

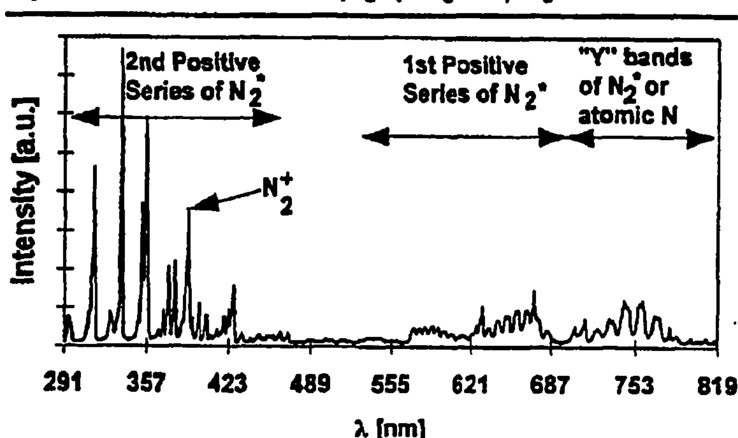

Figure B-4: Typical optical emission spectra obtained for nitrogen plasma

B.2.3 Effect of the Exit Aperture

The discharge area of the ECR source with the exit aperture employed in our research is shown schematically in Figure B-5. The aperture is a 1 mm thick boron nitride (BN) disc with a 1 cm diameter hole in the center, which is installed at the lip of the sources liner.

Due to the diameter of the discharge zone in the ECR source being smaller than the diameter for stable mode propagation, microwave launching into this region occurs below cutoff[3], confining the ECR condition to a region close to the thermal shield of the source. In order to analyze the aperture's effect on the pressure of the discharge region the flow conductances for both the exit aperture and the BN liner were calculated. The BN liner was approximated as a 2.54 cm diameter cylinder, 10 cm in length. The flow conductance of the

BN liner in the molecular flow regime can then be written as[6]

$$C = 12.1\frac{d^3}{l}[l/s] = 19.8[l/s] \qquad \text{(B-2)}$$

And the flow conductance for the aperture in the molecular flow regime is given by

$$C = 11.6A[l/s] = 9.1[l/s] \qquad \text{(B-3)}$$

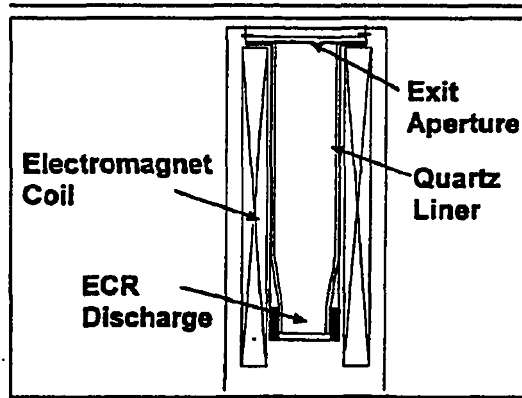

Figure B-5: ECR discharge tube with exit aperture

The pressure in the ECR zone with the exit aperture can be determined for a nitrogen flow of 6 sccm by first computing the effective conductance of both the liner and the aperture.

$$\frac{1}{C_{eff}} = \frac{1}{C_{aper}} + \frac{1}{C_{liner}}, C = 6.2[l/s]$$

(B-4)

$$P_{aper} = P_{\substack{grow \\ chamber}} + \frac{F_{N2}}{C_{eff}} = 12.4[mT]$$

Similarly, the flow conductances of the system without the aperture yields a much lower pressure in the ECR zone.

$$P_{\substack{no\\aper}} = P_{\substack{grow\\chamber}} + \frac{F_{N2}}{C_{liner}} = 4.0[mT] \qquad \text{(B-5)}$$

Therefore, the introduction of the exit aperture results in a pressure increase at the ECR discharge area by *at least* a factor of three over that without the exit aperture.

The exit aperture also has a significant effect on the diffusion of the various activated nitrogen species toward the substrate. The gas flow is limited mostly by the aperture resulting in a relatively small pressure drop within the source. An increase in neutral gas scattering inside the source occurs introducing a more significant pressure increase than that suggested by the calculated factor of three.

Furthermore, plasma induced gas heating causes a significant rarefaction of the gas within the ECR source. This has been shown to cause a pressure reduction by more than a factor of six at high power densities in larger systems.[7] Since the power density in this type of compact ECR' is typically high, even at low incident microwave powers, the effective pressure would be expected to be significantly reduced. However, as this plasma induced gas heating has been shown to diminish with increased gas pressure, it is expected that with the exit aperture, not only will the pressure be increased by the factor of three above, but also the stability of the source when it is operated at higher power levels will be enhanced.

A final phenomena affected by the exit aperture worth mentioning is referred to as *beam pumping,* and pertains to the effective pumping of gas out of the source through a process of gas ionization followed by extraction of these ions via grad-B diffusion along the magnetic field lines. In larger systems with magnetic mirror geometries, this effect is relatively insignificant.[7] However in this type of compact ECR, the single axial solenoid does not induce

such a confinement suggesting that this effect also plays a significant role in rarefying the gas at the ECR zone. This effect is expected to be more significant at lower pressures due to the longer mean free path of the gaseous species. It is clear that the exit aperture is an effective means of substantially increasing the pressure locally in the source where much of the ion's grad-B drift acceleration occurs. Therefore the exit aperture can potentially improve the properties of the films grown with such a source by reducing the kinetic energy of the charged species which collide with both the source and the chamber walls. Thus it is possible that the exit aperture suppresses the generation of impurities during the growth.

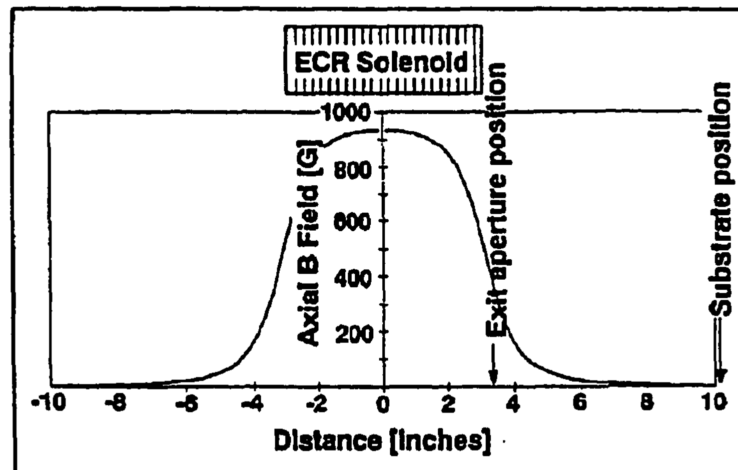

Figure B-6: Magnetic field strength along the axis of the ECR source's solenoid

It has been observed that the downstream ion energies in ECR plasmas diminish with process pressure[8], presumably through collisional losses with background gas species. The grad-B drift kinetic energy loss induced by gas collisions inside the source can be estimated by assuming that this component is nearly relaxed on the ion exiting the aperture and calculating the axial magnetic field via the expression

$$B(z) = \mu_0 \frac{Ni}{2d}\left[\frac{\frac{d}{2a}-\frac{z}{a}}{\sqrt{1+\left(\frac{d}{2a}-\frac{z}{a}\right)^2}}+\frac{\frac{d}{2a}+\frac{z}{a}}{\sqrt{1+\left(\frac{d}{2a}+\frac{z}{a}\right)^2}}\right] \quad \text{(B-6)}$$

Where Ni is the number of amp-turns, d is the length of the solenoid (6 inches) and a is the radius of the solenoid (1 inch). Figure B-6 indicates the magnetic field strength as a function of position along the axis of the ECR's solenoid. As can be seen, the magnetic field is approximately a factor of two less at the exit aperture than at the ECR condition suggesting that a substantial fraction of the plasma's ions acceleration along the field lines due to grad-B drift may be dissipated by collisions within the discharge cavity by using the aperture.

B.3 Fundamentals of ECR Electromagnetic Theory

B.3.1 The ECR Process

Plasma generation in this experiment is best understood by looking at a simple model of the ECR process.[9] The plasma generation region at the ECR source consists of an electromagnetic coil wound around a stainless steel tube and a microwave introduction window at one end of the tube. Due to the Lorentz force,

$$\bar{\mathbf{F}} = q\left(\bar{\mathbf{v}} \times \bar{\mathbf{B}}\right) \quad \text{(B-7)}$$

free electrons in this area spiral around a static magnetic field induced by the coil. The frequency of rotation (gyrotron frequency) is determined as follows. Due to the orientation of the induction coil, we can assume that $\bar{\mathbf{B}} = B_0\hat{a}_z$ and equation (II-7) becomes

$$m\frac{d^2x}{dt^2}\hat{a}_x + m\frac{d^2y}{dt^2}\hat{a}_y + m\frac{d^2z}{dt^2}\hat{a}_z = qB_0\left(v_y\hat{a}_x - v_x\hat{a}_y\right) \tag{B-8}$$

Thus the cross-product gives the following equalities

$$m\frac{d^2x}{dt^2} = qB_0v_y$$

$$m\frac{d^2y}{dt^2} = -qB_0v_x \tag{B-9}$$

$$m\frac{d^2z}{dt^2} = 0$$

By integrating from 0 to t we get

$$\frac{dx}{dt} = \frac{qB_0y}{m} + C_1$$

$$\frac{dy}{dt} = -\frac{qB_0x}{m} + C_2 \tag{B-10}$$

$$\frac{dz}{dt} = C_3$$

Recalling that velocity is the time-derivative of position, we can substitute these identities back into equation B-9, thus uncoupling the differential equations. By defining the following parameters for the equation in x,

$$\omega_0 = \frac{qB_0}{m} \text{ and } x_0 = \frac{C_2}{m\omega_0} \text{ we get}$$

$$\frac{d^2x}{dt^2} + x\omega_0^2 = x_0\omega_0^2 \qquad \text{(B-11)}$$

whose solution is

$$x = x_0 + R\cos(\omega_0 t + \phi) \qquad \text{(B-12}$$

where R and f are constants of integration. By taking the time derivative of B-12 we get the electron velocity in the x-direction.

$$v_x = \frac{dx}{dt} = -R\omega_0 \sin(\omega_0 t + \phi) \qquad \text{(B-13)}$$

Substituting this result back into equation B-10 also gives the electron velocity in the y-direction

$$y = y_0 - R\sin(\omega_0 t + \phi) \qquad \text{(B-14)}$$

and

$$v_y = \frac{dy}{dt} = -R\omega_0 \cos(\omega_0 t + \phi) \qquad \text{(B-15)}$$

where $y_0 = \frac{C_1}{m\omega_0}$. The motion of an electron in a plane perpendicular to the z-component of the magnetic field can be determined by squaring and adding equations B-12 and B-14 which results in a circle of radius R

$$(x-x_0)^2+(y-y_0)^2=R^2 \quad \text{(B-16)}$$

Equations B-13 and B-15 give us information to solve for the radius

$$R=\frac{\sqrt{v_x^2+v_y^2}}{\omega_0}=\sqrt{v_x^2+v_y^2}\left(\frac{m}{qB_0}\right) \quad \text{(B-17)}$$

Equation II-10 also tells us that the velocity in the z-direction is constant and that the electrons spiral around the z-axis with a radian frequency of

$$\omega_0=\frac{qB_0}{m} \quad \text{(B-18)}$$

The electron gyration and the microwaves are in resonance when ω_0 and the microwave radian frequency ($2\pi f_0$) are equal. Since the microwave source used in this work is preset at f_0=2.45 GHz then

$$\omega_0=2\pi\bullet 2.4\hat{5}\text{GHz}=\frac{qB_0}{m} \quad \text{(B-19)}$$

Thus the ECR condition is when the magnetic field intensity is 875 G.

Linearly polarized microwaves introduced into the ECR region propagate along the axis of the static magnetic field. A linearly polarized plane wave can be equivalently represented by two circularly polarized waves rotating in opposite directions. For instance, the electric field intensity of a linearly polarized microwave can be expressed as

$$\bar{E}=E_0\cos(\omega t)a_y \quad \text{(B-20)}$$

and can also be written as

$$\vec{E} = \mathrm{Re}\left[\frac{E_0}{2}(a_y + ja_x)e^{j\omega t} + \frac{E_0}{2}(a_y - ja_x)e^{j\omega t}\right] \tag{B-21}$$

where the components in the bracket are waves with right-hand circular polarization (RCP) and left-hand circular polarization (LCP) respectively.

II.3.2 The ECR Condition

The electron cyclotron resonance condition is achieved when the gyration frequency and the microwave frequency are equivalent. At this point the electrons and the electric field vector of the RCP microwaves are rotating in phase with each other and the energy of the RCP microwaves goes into accelerating the electrons. Since the electrons and the LCP electric field vector are rotating in opposite directions, electron cyclotron resonance cannot be the method of microwave power absorption for the LCP waves. Other possible energy loss mechanisms must be looked into for the LCP microwaves. There are many rather complex theories regarding the absorption of the LCP waves. The important result that comes out of the theories is that when the plasma density gets large enough, the LCP waves are almost completely absorbed. The point where this occurs is called the critical density, N_{cr}. When the density of the plasma exceeds N_{cr}, the microwaves are no longer able to propagate through the plasma (the amplitude decreases exponentially). By solving Maxwell's equations[10], the critical density is determined to be

$$N_{cr} = \frac{\omega^2 \varepsilon_o m_o}{q^2} \tag{B-22}$$

which results in a critical density of7.5 x 10^{10} cm^{-3} for the 2.45 GHz used in this work.

The spiraling high energy electron gas creates a long mean free path confined to a relatively short region. As we decrease the pressure, this long mean free path becomes necessary as the probability for a collision event also decreases.[10] Electron collisions with the neutral nitrogen gas molecules cause ionization and the formation of free radicals in the form of

atomic and ionic nitrogen. Thus we are able to efficiently generate a low pressure, high density plasma in the restricted confines of the MBE chamber.

The variable parameters in controlling the plasma consist of the flow rate of the nitrogen, the magnetic field strength, the microwave power and efficiency of the microwave coupling with the electron gyration. The flow rate determines the chamber pressure which was kept as low as possible while maintaining stoichiometric growth at as high a rate as possible. This chamber pressure was also sufficient to maintain the critical density necessary for stable plasma generation.

B.4. References

(1) Lei, T.; Fancuilli, M.; Molnar, R. J.; Moustakas, T. D.; Graham, R. J.; Scanlon, J. *Appl. Phys. Lett.* **1991**, *59*, 944-946.

(2) Molner, R. J.; Lei, T.; Moustakas, T. D. **1993**, *281*,

(3) Molnar, R. J.; Singh, R.; Moustakas, T. D. *Journal of Electronic Materials* **1995**, *24*, 275-281.

(4) III, J. E. H.; Paraszczak, J. R.; Moisan, M.; Sauve, G. *J. Vac. Sci. Technol.* **1987**, *B 5*, 347-354.

(5) Molnar, R. J.; Moustakas, T. D. *J. Appl. Phys.* **1994**, *76*, 1-9.

(6) *Vacuum Technology its Foundations, Formulae and Tables*; Leybold-Heraeus Vacuum Products Inc.: catalog, 1993.

(7) Rossnagel, S. M.; Schatz, K.; Whitehair, S. J.; Guarnieri, R. C.; Ruzic, D. N.; Cuomo, J. J. *J. Vac. Sci. Technol. A* **1991**, *9*, 702.

(8) Holber, W. M.; Forrester, J. *J. Vac. Sci. Technol. A* **1990**, *8*, 3720.

(9) Popov, O. *ECR Plasma Sources and their use in Thin Film Deposition*; (currently unpublished)

(10) DeBoer, S. J. Doctor of Philosophy Thesis, Iowa State University, 1995.

APPENDIX C
STATISTICAL DESIGN OF EXPERIMENT

C.1 DOE Method

Design of Experiments (DOE) is a methodology for systematically applying statistics to experimentation. This portion of the study employs ECHIP™ a commercially available software package designed for the optimization of multivariable process systems. DOE allows the experimenter to develop a mathematical model that predicts how input or control variables interact to create output variables or responses in a process or system. This model, which shows how these variables and responses interact, is produced through a sequence of experiments called a design. The design is generated by ECHIP when the key control variables as well as the desired responses are identified. In order to facilitate a valid experiment design, it is required that practical ranges of the input variables be known.

Table C-1: Key control variables for DOE

Control Variable	Minimum	Maximum
Buffer Layer Thickness	200 Å	800 Å
Substrate Temperature	450°C	600°C
ECR Microwave Power	25 W	85 W
ECR Magnet Current	13 A	18 A

For instance, initial experiments revealed that good quality III-V nitride films were grown when the ECR microwave power was set between 25 and 85 watts, even though the microwave generator ranges from 0 to 250 watts.

C.1.1 Independent variables

Based upon experience with the ECR-MBE system in our laboratory, the key variables and practical ranges of operation were identified and are listed in Table C-1. An understanding of the effect of these variables is necessary to understand and interrupt the results of the experiment.

- The buffer layer accommodates the lattice mismatch between the substrate and the nitride film.
- The substrate temperature determines the surface mobility of the adatoms and their ability to occupy lattice sites. This is further complicated by the fact that high surface temperatures cause re-evaporation of indium, thus affecting the In/Ga ratio.
- ECR microwave power controls the amount of atomic nitrogen required for stoichiometric growth. However high microwave power promotes ion damage to the film surface.
- Finally, the ECR magnet current controls the position of the ECR condition relative to the substrate surface. This can also affect the amount of ion damage to the film.

C.1.2 Responses/dependent variables

Initial (Ga,In)N films grown in our laboratory were characterized by two midgap photoluminescence peaks at about 2.67 eV and 2.47 eV, in addition to the expected excitonic peak at around 3.1 eV for $Ga_{0.8}In_{0.2}N$. Subsequent growths revealed that not only were the peak intensities affected by the control variables, but the relative intensities between the midgap peaks and the exciton peak were also affected by these parameters. Therefore it was determined that the most logical response variables were identified as the exciton peak and the midgap peaks.

C.1.3 Define objectives/design experiment

The objective, then, was to determine the effect of the growth conditions on the response variables. Once these relations were understood, one could decide what combination of control settings would minimize the midgap peaks and simultaneously maximize the exciton peak. This would insure that the photonic emissions would be associated with band to band type transitions rather than with trap or defect related transitions, hence better crystal quality.

Based on previous data and experience, it was determined that a nonlinear relationship between the control variables and the responses existed. There was also an interaction between the various controls. With this knowledge, a quadratic design with edge and center points was selected. This is a screening design that produces a simple quadratic model. Such models predict the primary effects between input variables and responses over the range of the settings

Table C-2: Experimental Conditions

Trial #	**Buff.Thcknss**	T_s	**MWP**	I_B
17	500	600	25	13
16	500	450	25	18
12	200	450	85	16
13	500	525	85	18
14	800	525	60	18
1	200	450	25	13
11	200	600	25	16
5	200	450	25	18
9	800	600	85	18
19	200	525	25	18
2	800	600	25	13
4	200	600	85	13
18	800	450	60	13
10	800	450	25	16
15	500	600	60	18
3	800	450	85	13
6	800	600	25	18
8	200	600	85	18
7	800	450	85	18
20	200	525	25	18

covered by the trials. The designed experiment, suggested by ECHIP, provided the information necessary with the minimal number of experimental trials to determine the effect of individual variables. The center points would gauge the amount of curvature in the model that resulted from the interaction among the variables.

C.1.4 Running the Experiment

As mentioned previously, minimum and maximum settings for each variable were based on experience. Middle settings were also selected for the center point. When the data for the settings of variables and decisions about the quadratic model with center points were entered into the system, the software called for a total of 25 trials. These trials consisted of 20 unique experimental runs with a repetition of 5 of these 20.

Repetition is a technique for statistically determining error. The settings for individual variables and the random sequence of the trials generated by the software is given in Table C-2, which shows the distribution of high and low settings for the 20 unique trials and the middle settings for the 4 center point replications.

Table C-3 shows the PL results of the 25 trials suggested by ECHIP, again, 1-20 are unique trials and 21-25 are repetitions of trials 1-5.

C.1.6 Analyzing the Results

After the data is entered into the system, the first consideration the model addresses is what variables have an effect on what responses. Table C-4 summarizes this information. The effects table compares the size of each effect to the amount of noise or random error in the system. The larger the effect, the more it stands out from the noise and the more stars it gets. The terms generated by the program contain quadratic as well as cross terms in addition to a constant term. The coefficients to these terms are statistically determined by the program to fit the experimental data. From this curve fit, the effects of simultaneously changing the variables can be extrapolated and the optimum settings can be determined without having data points for these particular parameters.

Table C-3: PL results; amplitude in mV

Trial#	Band Peak	Subband 1	Subband 2
1	65.6	7.6	4.8
2	76.4	2.2	3.5
3	67.3	9.1	4.1
4	64.1	11.2	7.9
5	39.6	17.2	18.4
6	31.2	19.4	22.1
7	18.3	17.5	20.7
8	10.1	16.3	16.2
9	51.3	17.4	12.8
10	58.2	11.5	9.4
11	47.6	15.3	14.1
12	27.6	18.9	20.0
13	16.4	16.9	18.7
14	35.3	19.2	20.1
15	54.1	13.2	13.3
16	43.7	15.9	16.2
17	73.6	2.8	4.1
18	71.8	3.7	4.1
19	60.8	13.6	8.3
20	20.5	19.5	22.3
21	64.7	7.4	4.7
22	76.7	2.7	3.2
23	64.1	8.6	4.4
24	61.8	11.7	8.1
25	41.3	16.9	18.7

Table C-4: Effects of variables

Band	Sub 1	Sub2	Quadratic and Cross Terms
*	-	-	Buffer thknss^2
-	-	-	SubstrTemp^2
***	-	-	MW Pwr^2
***	***	***	Mag Current^2
*	-	-	Buffer thknss*SubstrTemp
-	-	-	Buffer thknss*MW Pwr
-	**	-	Buffer thknss*Mag Current^
-	-	-	SubstrTemp*MW Pwr
-	-	-	SubstrTemp*Mag Current
***	**	-	MW Pwr*Mag Current

The key variables which had the most significant effect on the response variables were the current to the ECR magnetic coil and the power to the ECR microwave generator (Table C-4). A key tool for detailed analysis of the experimental results is the contour plots generated by ECHIP. Each plot, which is presented in both two and three dimensions, shows a valuable visualization of how these key variables interact at different settings (Figure C-1). ECHIP is capable of showing any combination of control variables and their combined effect on the response variables. It is also capable of determining the combined effect of all four control variables and thus predicting an optimal setting scheme for the entire system which would produce the best quality (Ga,In)N single crystal thin films. The predicted optimal settings were as follows;

- Buffer layer thickness = 600Å
- Substrate Temperature = 600°C
- ECR Microwave Power = 40 W
- ECR magnet Current = 13 A

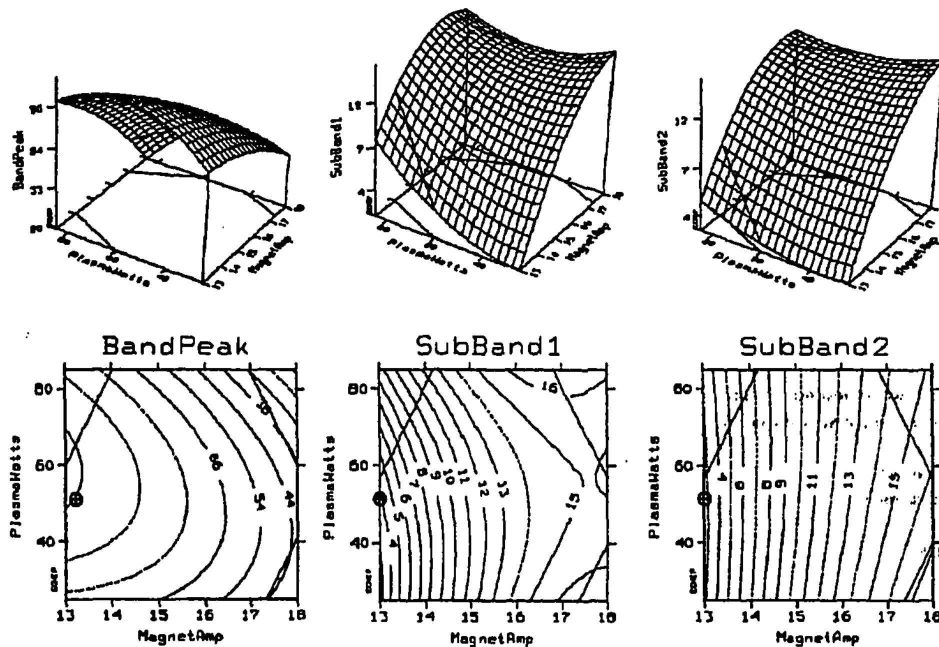

Figure C-1: Response surfaces in 3D and contour plots.

We decided to challenge the predictions suggested by ECHIP by growing three samples at or near these settings and comparing the results. The settings and results are presented in Table C-5.

Table C-5: Results of optimized control settings

Trial	Buff	T_s	MWP	I_B	Band Peak	Subband 1	Subband 2
1	590	600	40	14	71.3	4.7	2.1
2	600	590	35	13	96.2	3.6	2.4
3	600	600	40	13	97.1	3.4	2.3

These results demonstrate that ECHIP's predictions were very accurate in determining the proper parameters and setting the stage for optimizing our growth process. These parameter settings were used in all subsequent growths and proved reliable throughout the remainder of the experiment. However, when we varied the In/Ga ratio, the quality of the material became less consistent suggesting that these optimized growth parameters are valid only for the Ga-rich regime. Further DOE experiments are required to optimize growth of In-rich material.

APPENDIX D
X-RAY DIFFRACTION

D.1. Diffraction

Diffraction is due essentially to the existence of certain phase relations between two or more waves. Differences in the paths traveled by the individual waves lead to shifts in phase and these phase differences subsequently lead to changes in amplitude[1]. For instance, two polarized, equal amplitude, monochromatic waves whose paths differ by one half wavelength will produce a wave of zero amplitude and if their path lengths differ by zero or by a whole number of wavelengths the resulting amplitude will be the sum of the constituent wave amplitudes.

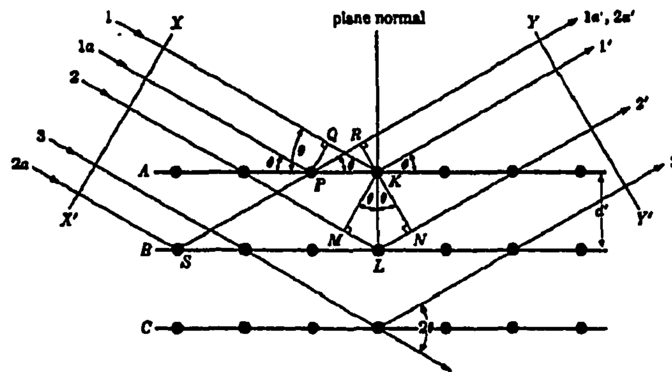

Figure D-1: Diffraction of x-rays by a crystal

Differences in the path length of various waves arise quite naturally when we consider how a crystal diffracts x-rays. Figure D-1 shows a section of a crystal, its atoms arranged on a set of parallel planes A,B,C,D,....,normal to the plane of the drawing and spaced a distance d' apart.

Assume that a beam of perfectly parallel, perfectly monochromatic x-rays of

wavelength λ is incident on this crystal at an angle θ which is measured between the incident beam and the particular crystal planes under consideration. We want to know if this beam will be diffracted and if so, under what conditions. *A* diffracted beam may be defined as a beam composed of a large number of scattered rays mutually reinforcing one another. [1] Diffraction is therefore a scattering phenomenon and not one involving any "new" kind of interaction between x-rays and atoms.

For the particular conditions described by Figure D-1 the only diffracted beam formed is that shown, specifically the one making an angle θ of reflection equal to the angle θ of incidence. This is shown, first, for one plane of atoms and, second, for all the atoms making up the crystal. Consider rays **1** and **1a** in the incident beam; they strike the atoms K and P in the first plane of atoms and are scattered in all directions. Only in the directions 1' and 1a', however, are those scattered beams completely in phase and so capable of reinforcing one another; they do so because the difference in their length of path between the wave fronts XX' and YY' is equal to

$$QK - PR = PK \cos\theta - PK \cos\theta = 0 \qquad \text{(D-1)}$$

Similarly, the rays scattered by all the atoms in the first plane in a direction parallel to **1'** are in phase and add their contributions to the diffracted beam. This will be true of all the planes separately, and it remains to find the condition for reinforcement of the rays scattered by atoms in the different planes. Rays **1** and **2**, for example, are scattered by atoms K and L, and the path difference for rays **1K1'** and **1L1'** is

$$ML + LN = d' \sin\theta + d' \sin\theta \qquad \text{(D-2)}$$

This is also the path difference for the overlapping rays scattered by S and P in the direction shown, since in this direction there is no path difference between rays scattered by S and L or P and K. Scattered rays **1'** and **2'** will completely in phase if this path difference is equal to a whole number n of wavelengths, or if

$$n\lambda = 2d' \sin\theta \qquad \text{(D-3)}$$

This relation was first formulated by W. L. Bragg and is known as Braggs law. It states the essential condition which must be met if diffraction is to occur. n is called the order of the reflection; it may take on any integral value consistent with sin θ not exceeding unity and is equal to the number of wavelengths in the path difference between rays scattered by *adjacent* planes. Therefore, for fixed values of λ and d', there may be several angles of incident θ_1, θ_2, θ_3.... at which diffraction may occur, corresponding to n = 1, 2, 3,....

The rays scattered by all the atoms in all the planes are therefore completely in phase and reinforce one another (constructive interference) to form a diffracted beam in the direction shown. In all other directions of space the scattered beams are out of phase and annul one another (destructive interference). The diffracted beam is rather strong compared to the sum of all the rays scattered in the same direction, simply because of the reinforcement which occurs, but extremely weak compared to the incident beam since the atoms of the crystal scatter a small fraction of the energy incident on them[1].

D.2 The Bragg Law

Two geometrical considerations are (1) The incident beam, the normal to the reflecting plane, and the diffracted beam are always coplanar. (2) The angle between the diffracted beam and the transmitted beam is always 2θ. This is known as the diffraction angle, rather than θ, which is usually measured experimentally.

Diffraction, in general, occurs only when the wavelength of the wave motion is of the same order of magnitude as the repeat distance between scattering centers. This requirement follows from the Bragg law. Since sinq cannot exceed unity, we may write

$$\frac{n\lambda}{2d'} = \sin\theta < 1 \qquad \text{(D-4)}$$

Therefore nl must be less than 2d'. For diffraction, the smallest value of n is 1. Therefore the condition for diffraction at any observable angle 2θ is

$$l < 2d' \qquad \text{(D-5)}$$

The Bragg law may be written in the form

$$\lambda = 2\frac{d'}{n}\sin\theta \qquad \text{(D-6)}$$

Since the coefficient of λ is now unity, we can consider a reflection of any order as a first-order reflection from planes, real or fictitious, spaced at a distance 1/n of the previous spacing. This turns out to be a real convenience, so we set d = d'/n and write the Bragg law in the form

$$\lambda = 2d\sin\theta \qquad \text{(D-7)}$$

In order to determine all of the possible directions, i.e., the possible angles 2θ, in which a given crystal can diffract monochromatic x-rays, we must consider the d spacing between the parallel planes since there are many orientations which can expose a particular plane. Simple geometry gives us the following relations for cubic and hexagonal lattices respectively

$$\frac{1}{d^2} = \frac{\left(h^2 + k^2 + l^2\right)}{a^2}$$

and (D-8)

$$\frac{1}{d^2} = \frac{4}{3}\left(\frac{h^2 + hk + l^2}{a^2}\right) + \frac{l^2}{c^2}$$

Combining these individually with equation D-7 gives

$$\sin^2\theta = \frac{\lambda^2}{4a^2}\left(h^2 + k^2 + l^2\right)$$

and (D-9)

$$\sin^2\theta = \frac{\lambda^2}{4}\left\{\frac{4}{3}\left(\frac{h^2 + hk + k^2}{a^2}\right) + \frac{l^2}{c^2}\right\}$$

These equations predict, for a particular incident wavelength λ and a particular unit cell size a and c, all the possible Bragg angles at which diffraction can occur from the planes (hkl)[1]. Similar equations can readily be obtained for other crystal systems. Thus diffraction directions are determined solely by the shape and size of the unit cell. We can thus determine an unknown crystals shape and unit cell size by measurements of the direction of the diffracted x-ray beams.

D.3. Diffractometry

By using x-rays of known wavelength λ and measuring 2θ, we can determine the spacing d of various planes in a crystal. The essential features of a diffractometer are shown in Figure D-2. X-rays form the tube T are incident on the crystal C which may be set at any desired angle to the incident beam by rotating about an axis through O, the center of the diffractometer circle.

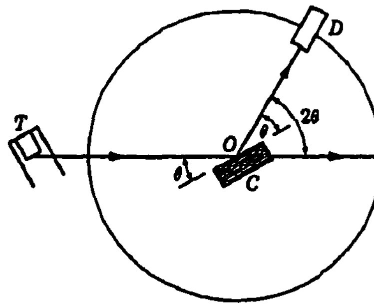

Figure D-2: The x-ray spectrometer

D is a counter which measures the intensity of the diffracted x-rays; it can also be rotated about O and set at any desired angular position. The mechanism which controls the specimen and detector rotation is called a *goniometer.* In use, the crystal rotates through continuous values of θ while the detector simultaneously rotates through the corresponding angle 2θ. Thus the measured intensity of the diffracted beam is plotted for all values of θ; this is called a *θ-θq scan.*

The relation between destructive interference and structural periodicity can be further illustrated by a comparison of x-ray scattering by solids, liquids and gases (Figure D-3). The curve of scattered intensity vs. 2θ for a crystalline solid is almost zero everywhere except at certain angles where high sharp maxima occur: these are the diffracted beams. Both amorphous solids and liquids have structures characterized by an almost complete lack of

periodicity and a tendency to "order" only in the sense that the atoms are fairly tightly packed together and show a statistical preference for a particular interatomic distance; the result is an x-ray scattering curve showing nothing more than one or two broad maxima. Finally, there are the monatomic gases, which have no structural periodicity whatsoever; in such gases, the atoms are arranged perfectly at random and their relative positions change constantly with time. The corresponding curve shows no maxima, merely a regular decrease of intensity with increase in scattering angle. The curve would be featureless except for the fact that isolated atoms tend to scatter x-rays more intensely at low 2θ angles than at high[1].

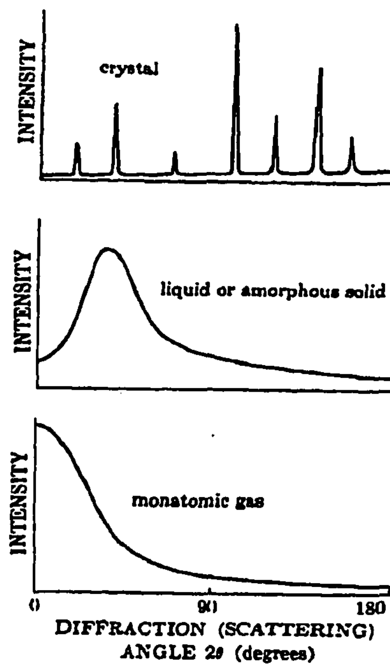

Figure D-3: Comparative x-ray scattering by crystalline solids, amorphous solids, liquids, and monatomic gases (schematic).

D.4. Rocking Curves

In the previous derivation we assumed certain ideal conditions; namely a perfect crystal and an incident beam composed of perfectly parallel and strictly monochromatic radiation.

These conditions never actually exist. For example, the "monochromatic" beam produced in the laboratory is simply one containing the strong $K\alpha$ component superimposed on the continuous spectrum. But the $K\alpha$ line itself has a width of about 0.001Å and this narrow range of wavelengths leads to significant line broadening, i.e. of measurable diffraction at angles close, but not equal, to the actual Bragg angle. Also, real crystals are imperfect simply because they are not infinite. There is also a kind of crystal imperfection known as a mosaic structure which is possessed by all real crystals to a greater or lesser degree and which has a decided effect on diffraction phenomena. It is a kind of substructure into which a single crystal is broken up and is illustrated in Figure D-4 in an enormously exaggerated fashion. A crystal with mosaic structure does not have its atoms arranged on a perfectly regular lattice extending from one side of the crystal to the other; instead, the lattice is broken up into a number of tiny blocks, each slightly disoriented from another.

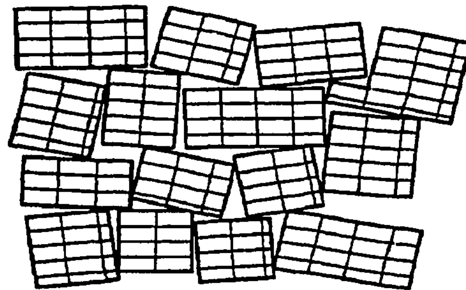

Figure D-4: Mosaic structure of a real crystal

The quality of what is nominally a "single " crystal can vary over an enormous range. At one extreme, the crystal may exhibit gross plastic deformation by bending and/or twisting such that some portions of it are disoriented from other portions by angles as large as tens of degrees and the dislocation density is high.

In the case of the metallurgist or the material scientist, the amount and direction of stress in construction material are important data relating to reliability (maximum load) and

lifetime (fatigue) of constructions, machines, engine parts and so on. It is also of equal importance to know the stress in materials between subsequent steps in the production process.

At the other extreme, some carefully grown crystals are almost free of dislocations and other line or planer imperfections, and their crystal planes are flat to less than 10^{-4} degrees over distances of the order of a centimeter. In general, metal crystals tend to be more imperfect than crystals of covalent or ionic substances. Various methods of x-ray diffractometry are available to assess crystal quality. These methods differ in sensitivity and resolution and the type of measurement used depends mainly on the allowable tolerances as well as the particular material application[1].

The powder method of x-ray diffraction involves the diffraction of monochromatic x-rays by a powder specimen "Powder" can mean either an actual, physical powder held together with a suitable binder or any specimen in polycrystalline form. The technique is thus eminently suited for metallurgical work, since single crystals are not always available to the metallurgist and such materials as polycrystalline wires, sheet, rod, etc., may be examined nondestructively without any special preparation.

In the powder method, the diffracted beams lie on the surfaces of cones whose axes lie along the incident beam or its extension; each cone of rays is diffracted from a particular set of lattice planes. The diffractometer has the ability to measure the positions and the intensities of diffracted lines simultaneously and quickly. In these applications, resolution on the order of a degree are sufficient to analyze materials for construction purposes. However, extremely low concentrations of misfit dislocations, vacancies, and impurities have drastic effects on the electrical and optical properties of single crystals while the structural properties remain unchanged[1]. Also, in analyzing semiconductor heterostructures, very often nearly lattice matched materials are used requiring much higher resolution than that used for typical residual stress analysis. Clearly, the collimation of the incident beam and the stepping size of the goniometer must all be consistent with peak widths and separations of a few seconds of arc.

There two instrumental approaches to this problem; each have their own particular advantages. There are the double crystal diffractometer (DCD) and the five crystal diffractometer and to begin with, there are three fundamental requirements for both. The first, and most obvious, is the requirement for very high stepping accuracy on the sample or theta axis. The step size must be on the order of one arc second. This is a matter of appropriate engineering and can be achieved using a reduction gearbox on the worm drive of a high quality goniometer or else a tangent arm driven by a micrometer. The later is capable of extremely high accuracy, but only over a limited angular range[2].

The second requirement is for very good angular collimation of the incident x-ray beam. The angular divergence of this beam should be less than 10 arc seconds. It is not possible to achieve this using conventional *slit-type* collimation, but collimation by diffraction from a highly perfect crystal gives a beam with the correct characteristics.

The third requirement is to eliminate peak broadening due to spectral dispersion. The Cu $K\alpha 1$ characteristic line has a certain intrinsic width, or delta l[2]

Cu K alpha = 1.54051 Å

FWHM = 0.00046 Å (=0.03%)

and, of course, the Cu $K\alpha 2$ component must also be considered.

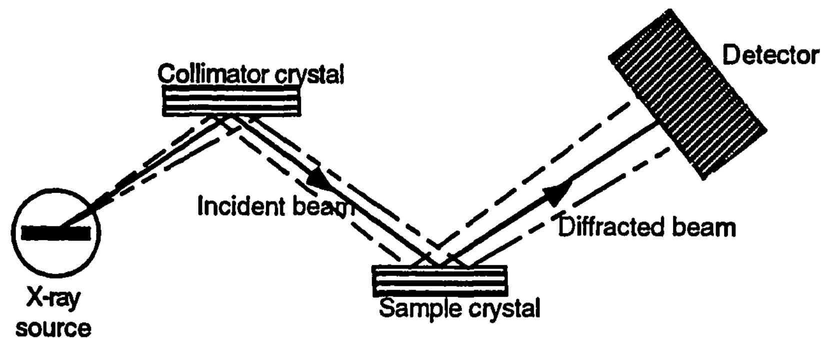

Figure D-5: Schematic of a Double-Crystal Diffractometer

There are two ways to eliminate peak broadening due to spectral dispersion. The first is to use a double-crystal diffractometer, in which the first crystal (or collimator crystal) is of the same material as the second (or sample) crystal. A schematic diagram of a double-crystal

diffractometer is shown in Figure D-5. The source, say the point focus of a sealed Cu anode x-ray tube, emits a full spectrum of x-radiation, including the $K\alpha 1$, and $K\alpha 2$ doublet. The first crystal is set at the correct Bragg angle for the$K\alpha$ line. The diagram shows three beam paths, representing different wavelength components of the $K\alpha$ line. The solid line represents a medial wave length, whereas the dashed line represents a longer wavelength component and the chain-dashed a shorter. Note that all three components are diffracted simultaneously by the crystal, but from slightly different points on the crystal surface.

The second (or sample) crystal sits on the goniometer theta axis and, when it satisfies the Bragg condition for the median (solid) wavelength component, it lies precisely parallel to the first crystal. But note that it also satisfies the Bragg condition for the longer and shorter wavelength components. This means that, as the sample is rotated on theta, during a rocking curve measurement, it can simultaneously satisfy the Bragg condition for all the wavelength components emitted by the source. There is no peak broadening due to spectral dispersion. This is known as the (1,-1) focusing condition[2].

Clearly, if the symmetry of this condition is broken, say by changing to another sample material with a different 'd' spacing, the sample crystal will not diffract all of the wavelength components simultaneously and we will see peak broadening. The double-crystal diffractometer, therefore, has serious limitation. It can only be used to study one particular Bragg reflection from one particular sample material. To change sample materials means to change the first crystal, and in the case of III-V nitrides, it is difficult to obtain a perfect crystal specimen for the collimating crystal. It does have one enormous advantage, however. Since the entire $K\alpha 1$, $K\alpha 2$ doublet is used, the diffractometer makes very efficient use of the source.

The inherent limitation if the double-crystal diffractometer, its lack of versatility, can be overcome by employing a four crystal monochrometer. This device produces an extremely monochromatic x-ray beam (some 5% of the intrinsic width of the $K\alpha_1$ line) and so eliminates spectral dispersion over the entire angular range[2]. This is the 5 crystal diffractometer and is

schematically represented in Figure D-6. The monochrometer is comprised of two 'U' shaped blocks of highly perfect crystals. The blocks are cut in such a way that either the (440) or (220) reflections can be used. Note that the first pair of crystals act as a double-crystal diffractometer, allowing the whole spectral distribution to pass. The third crystal, however, is set in a non-parallel way, and only a small range of wavelengths can satisfy the Bragg condition for any fixed angle. The forth crystal reflects the monochromatic beam back onto its original direction.

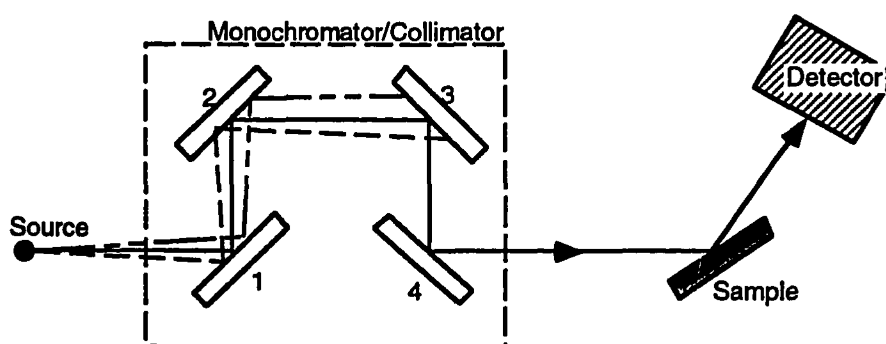

Figure D-6: Schematic of a 5-Crystal Diffractometer

The range of wavelengths passed is related to the intrinsic rocking curve width of the reflection used at the third crystal. For Ge (440) this is 5 arc seconds, and this allows some 5% of the characteristic line to pass. For the Ge (220) setting, the intrinsic rocking curve width is 12 arc seconds, and this allows some 25% of the characteristic line to pass[2]. This configuration gives a beam with poorer resolution, but with much higher intensity.

Using the (440) monochrometer setting, the resolution of the five-crystal diffractometer remains constant over almost the entire, usable two-theta range: from 0 to 150 degrees. Even in the lower resolution (220) configuration, the resolution remains essentially constant over a very wide angular range. By contrast, the resolution of the double-crystal diffractometer is good only over a very limited range of angles. These advantages come at the expense of

intensity. In comparison to the double-crystal diffractometer, the use of a four crystal monochrometer in the (220) setting results in an intensity loss of a factor of roughly 4. The high-resolution (440) setting gives a further intensity loss of about 20^2.

The double-crystal diffractometer, when used with the conventional sealed x-ray tube, gives a remarkably high-intensity signal. The double crystal x-ray optics are highly efficient. On the other hand, even with the intensity loss in the four crystal monochrometer, the beam intensity is quite sufficient for most applications. For the study of thin films or very weak scattering effects, it is possible to change to the (220) monochrometer setting. Furthermore, the intensity loss is largely compensated for by the very much lower instrumental background obtained when using the four crystal monochrometer.

D.5. References

(1) Cullity, B. D. *Elements of X-Ray Diffraction*; Addison-Wesley: Menlo Park, 1978.

(2) Ryan, T. In *Philips Analytical*; 1993.